

# Weather Regimes and Preferred Transition Paths in a Three-Level Quasi-Geostrophic Model

D. Kondrashov<sup>1</sup>, K. Ide, and M. Ghil<sup>2</sup>

Department of Atmospheric Sciences and  
Institute of Geophysics and Planetary Physics  
University of California, Los Angeles

*Revised version*

*J. Atmos. Sci., sub judice*

August 26, 2003

<sup>1</sup>*Corresponding author address:* Dr. Dmitri Kondrashov, Department of Atmospheric Sciences and Institute of Geophysics and Planetary Physics, University of California, Los Angeles, 405 Hilgard Ave., Los Angeles, CA 90095-1565. E-mail: dkondras@atmos.ucla.edu

<sup>2</sup>Additional permanent address: Département Terre-Atmosphère-Océan and Laboratoire de Météorologie Dynamique, Ecole Normale Supérieure, F-75231 Paris Cedex 05, FRANCE

## Abstract

Multiple flow regimes are reexamined in a global, three-level, quasi-geostrophic model with realistic topography in spherical geometry. This QG3 model, using a T21 triangular truncation in the horizontal, has a fairly realistic climatology for Northern Hemisphere winter, and exhibits multiple regimes that resemble those found in atmospheric observations. Four regimes are robust to changes in the classification method,  $k$ -means vs. mixture modeling, and its parameters. These regimes correspond roughly to opposite phases of the Arctic Oscillation (AO) and the North Atlantic Oscillation (NAO), respectively.

The Markov chain representation of regime transitions is refined here by finding the preferred transition paths in a three-dimensional (3-D) subspace of the model's phase space. Preferred transitions occur from the positive phase of the NAO ( $NAO^+$ ) to that of the AO ( $AO^+$ ), from  $AO^+$  to  $NAO^-$ , and from  $NAO^-$  to  $NAO^+$ , but not directly between opposite phases of the AO. The angular probability density function (PDF) of the regime exits that correspond to these preferred transitions have one or, sometimes, two fairly sharp maxima. These angular PDF maxima are, in most cases, not aligned with the line segments between regime centroids in phase space and might point to heteroclinic or homoclinic connections between unstable equilibria in the model's phase space. Preferred transitions paths are determined also for a stochastically forced Lorenz system, to help explain this striking feature of the QG3 model.

The episodic description of the model's low-frequency variability via the Markov chain of multiple regimes is complemented by an oscillatory description. Multi-channel singular-spectrum analysis is applied to the trajectory in the same 3-D subspace. Two statistically significant oscillations are found and have periods of 19 and 37 day, respectively. Both oscillations have four composites that include  $NAO^+$ ,  $AO^+$  and  $NAO^-$ , in this order. The fourth composite occurs between  $AO^+$  and  $NAO^-$ ; it resembles the Pacific–North-American

pattern, which is not captured by the model's episodic description. The two oscillations, in spite of the similarity of their spatial patterns, do not seem to be phased-locked. They have certain features in common with the westward-propagating Branstator-Kushnir wave, as well as with the standing oscillation that arises from the oscillatory topographic instability of Ghil and associates.

# 1 Introduction and motivation

Numerous studies of atmospheric observations have shown that low-frequency variability (LFV) is characterized by the existence of large-scale persistent and recurrent flow patterns, also called weather regimes. Weather regimes can be objectively identified in model results, as well as in observations, using various classification or clustering methods (see Table 1 in Ghil and Robertson 2002). The dominant regimes of Northern Hemisphere (NH) wintertime circulation are most often identified as the Pacific/North American (PNA) pattern, the reverse PNA (RNA), the North Atlantic Oscillation (NAO), and the Arctic Oscillation (AO). The positive and negative phases of the NAO correspond to zonal and blocked flow in the Atlantic sector, in the same way the PNA and RNA do so over the Pacific sector of the NH. The AO (Thompson and Wallace 1998; Wallace 2000) is a hemispheric, annular mode that has been strongly associated with the sectorial NAO.

Marshall and Molteni (1993) introduced a spectral, three-level, quasi-geostrophic (QG3) model in spherical geometry and showed that it has a fairly realistic NH winter climatology; it also exhibits multiple weather regimes that resemble those found in observations. These authors computed so-called neutral vectors that have the smallest time derivative, by linearizing the model's equations around its mean state. These neutral vectors were shown to be associated with the subspace of the system's phase space in which two quasi-stationary states are located. The long-time integration of the full QG3 model with a specially chosen forcing generated weather regimes similar to those defined by the neutral vectors.

The QG3 model has been widely used for studies of NH atmospheric LFV. Corti et al. (1997) analyzed leading NH teleconnections patterns and blocking from a long run of the QG3 model. The forcing sources in this run were computed using the ECMWF objective analyses of the streamfunction field in wintertime and the condition of zero tendency for the potential vorticity. The model reproduced the observed wintertime mean state, as well as low-

frequency and high-frequency variations of the atmospheric streamfunction field. Both the PNA and the NAO patterns were realistically simulated; the statistics of blocking frequency and duration in the Euro-Atlantic and Pacific sectors compared also reasonably well with the observations. Molteni and Corti (1998) investigated the dynamical origin of long-term variations in the statistical properties of the QG3 model's LFV.

D'Andrea and Vautard (2001) and D'Andrea (2002) analyzed the correspondence between global quasi-stationary states found in a low-order model and the QG3 model's weather regimes, as identified by cluster analysis. Their low-order model was constructed by projecting the equations on a few leading EOFs of the QG3 model. These authors found the flow-dependent parameterization of a closure term to be essential for the good performance of their low-order model. Given such a closure, approximate correspondence between the QG3 weather regimes and quasi-stationary states of the low-order model was obtained.

Extended-range weather prediction depends in a crucial way on skill at forecasting the duration of a regime event or other persistent anomaly, which is under way at initial forecast time, and the subsequent onset of another persistent anomaly, after the break of the current one (Ghil 1987). We use the QG3 model to address extended-range predictability in terms of the multiple-regime paradigm (Ghil and Robertson 2002). Our main purpose is to describe more precisely the preferred transition paths between regimes.

In section 2, the model is described briefly. In section 3 we identify robust weather regimes by two independent clustering methods, *k*-means (Michelangeli et al. 1995) and Gaussian mixture modeling (Smyth et al. 1999). In section 4, we show that highly significant transitions take place along preferred paths in a low-dimensional phase space. For better understanding, we also examine in Appendix A the preferred transitions paths in a stochastically forced Lorenz (1963a) system; in this case, the paths can be fully explained using known dynamical properties of the underlying nonlinear system.

In section 5 we complement the episodic description of the model’s LFV, as given in sections 3 and 4, by an oscillatory one: multi-channel singular-spectrum analysis is used to identify intraseasonal oscillations and connect them with the Markov chain of transitions between regimes. In section 6, we argue that the preferred transitions paths demonstrated in the QG3 model suggest that a similar analysis of numerical weather prediction models could help forecast regime breaks and subsequent onsets. To do so would require an efficiently designed observational system that is able to track spatial signatures of regime transitions.

## 2 Atmospheric model

The global model of Marshall and Molteni (1993) is governed by the equations for conservation of potential vorticity at the 200, 500 and 800 hPa pressure levels, written in shorthand notation as

$$\frac{\partial q}{\partial t} = -J(\psi, q) - D(\psi) + S; \quad (1)$$

here  $t$  is time,  $\psi$  is the streamfunction,  $q$  the potential vorticity,  $J$  the quadratic Jacobian operator, and  $D$  represents linear dissipation, in particular Newtonian cooling, Ekman dissipation on the 800 hPa wind, and hyperviscosity. The drag coefficients depend on the nature of the underlying surface. The model uses an expansion in spherical harmonics with a triangular truncation of T21 and realistic topography. The gridpoint values of the topography and sea-land mask represent averages over areas of 1000 km<sup>2</sup>.

Equation (1) is forced by time-independent, but spatially varying sources  $S$  of potential vorticity. These sources represent the average effects of diabatic heating and advection by divergent flow, and are determined from a condition requiring that, for a given climatological data set of observed fields, the time derivatives of vorticity vanish. The dataset of observed fields is given by ECMWF analyses of the streamfunction field at the three levels of the QG3 model, for the two winter months January and February, from 1984 to 1992. With

this forcing, the QG3 model reproduces the observed climatology of the underlying dataset, as well as providing good simulations of wintertime midlatitude variability. Marshall and Molteni (1993) and Corti et al. (1997) provide details of the model and of its performance.

### 3 Cluster analysis

The dataset for this analysis was obtained from a 54,000-day perpetual-winter simulation of our QG3 model. In order to examine robust features of the model’s phase-space structure, it is necessary to reduce the dataset’s dimensionality. For this purpose, we apply empirical orthogonal function (EOF) analysis to the unfiltered 500-hPa level streamfunction anomalies in the model’s NH. The anomaly field is sampled once a day and the data points are weighted by the cosine of their latitude.

The spatial patterns of the leading EOFs (not shown) are similar to those obtained by Corti et al. (1997) and by D’Andrea and Vautard (2001). The ten leading EOFs are responsible for 51% of the variance of the dataset: the first mode captures 12.5%, the second one 6.5%, the third one 5.2%, and the tenth one 3.1%. There is a slight break of slope in the variance curve after EOF-4, with the following eigenvalues forming a rather flat spectrum; the cumulative variance captured by the leading four EOFs equals 29%. Analyzing the streamfunction fields at the 250-hPa and 800-hPa levels (not shown) reveals very similar leading EOF patterns; this similarity indicates a predominantly barotropic structure of the model’s LFV, captured by the leading EOFs of the unfiltered data, with a finer structure present at the lower pressure level.

In order to objectively identify weather regimes in the QG3 model simulation, we apply two independent clustering methods (see Table 1 of Ghil and Robertson 2002) and compare the results. One method uses the  $k$ -means algorithm of Michelangeli et al. (1995) and the other uses the Gaussian mixture model of Smyth et al. (1999). Both these studies applied

their respective methods to the classification of NH weather regimes in observed geopotential height fields.

For a given number  $d$  of leading EOFs, both methods provide a number of clusters  $k$  and the cluster centroids in a  $d$ -dimensional subspace of the model's phase space. We want each cluster to correspond to a weather regime of the QG3. Therefore it is critical for our study to optimize the classification into clusters over various subspaces. The number of EOFs  $d$  and clusters  $k$  can be used as parameters to measure the robustness of the classification, along with diagnosing the similarity of the patterns themselves.

The  $k$ -means algorithm is based on the dynamic cluster method and formulated as follows. Given a prescribed number  $k$  of clusters in a  $d$ -dimensional space, it attempts to find an optimal partition of the data into the  $k$  clusters that minimizes the sum of the variances within each cluster. A data point belongs to a cluster if its distance to the cluster centroid is less than one standard deviation of all distances within a cluster. In order to determine the optimal  $k$ , Michelangeli et al. (1995) proposed the use of a classifiability index. This index measures the stability of the cluster solutions as a function of  $k$ , across different initial (random) seeds of the algorithm, based on the correlation between the cluster centroids. Table 1 gives the classifiability index of our QG3 model simulation for  $2 \leq d \leq 5$ . Clearly, it is very high for both  $k = 3$  and  $k = 4$ ; it follows that, based on this classifiability index alone, we cannot identify the optimal set of clusters in the QG3 model.

Table 1
---------

The Gaussian mixture model uses a linear combination of  $k$  Gaussian density functions, and differs from the  $k$ -means algorithm in the following two important aspects. First, each data point in the  $d$ -dimensional space can have a degree of membership in several clusters, depending on its position with respect to the centroid and the weight of a cluster (Smyth et al. 1999; Hand et al. 2001). Second, the mixture model has a built-in criterion for determining the optimal number of clusters supported by the data. This criterion is based

Table 2

on the cross-validated log-likelihood, shown in Table 2: the higher its algebraic value for a given dimension  $d$ , the more likely it is that  $k$  is the correct number of clusters for that  $d$ .

The mixture model consistently gives log-likelihood curves that saturate at  $k \geq 3$  and have a very weak maximum. Thus we can choose either  $k=4$  or  $k=5$  as the optimal number of clusters, according to this method. Hannachi and O'Neill (2001) found that when the data are not Gaussian, the mixture model tends to overfit them, so that the apparently optimal number of clusters increases with the length of the dataset. This seems to be the case here, too. In fact, when using 54,000 data points (see Table 3), rather than the 18,000 points of Table 2, the cross-validated log-likelihood curves have a tendency to saturate at higher values of  $k$ .

Table 3

Since the cross-validated log-likelihood of Smyth et al. (1999) supports both  $k=4$  and  $k=5$ , while the classifiability index of Michelangeli et al. (1995) supports either  $k=3$  and  $k=4$ , we compare the anomaly maps of the centroids produced by both methods (see, for instance, Table 2 in Robertson and Ghil 1999) in order to choose the optimal number of clusters. To do so, we compute the pattern correlation coefficients of the cluster centroids in physical space for pairs of visually similar streamfunction anomaly maps produced by the two clustering methods and compare the results for different values of  $k$ . We obtain the maps that correspond to the cluster centroids in the  $d$ -dimensional subspace by computing the EOF expansion of the 500-hPa streamfunction field, that is the QG3 model's second level, truncated at a particular value of  $d$ .

Table 4

Table 4 shows the correlation coefficients between corresponding pairs of clusters obtained from either method. Agreement between the two methods is very good for all values of  $d$  when using  $k=4$  (Table 4b), while for  $k=5$  (Table 4c) we find that only four of the clusters correlate well. The numerical correlation values are as good or better when using  $k=3$  (Table 4a); in this case, however, the actual patterns (not shown) do not match as well

those that were identified in previous work by other methods and from actual observational datasets as dominating NH LFV [see also the discussion in Smyth et al. (1999) and Ghil and Robertson (2002)].

Therefore we choose  $k=4$  as the optimal set of clusters for our QG3 model. The probability density function (PDF) based on the mixture model for  $d=3$  and  $k=4$  is shown in Figure 1, in the phase plane spanned by principal components (PCs) 1 and 2 (panel a), and by PCs 1 and 3 (panel b). All PCs are normalized by the standard deviation of PC-1. The coordinates of the cluster centroids for  $d=3$  are given in the figure caption; in higher dimensions ( $d \geq 4$ ) they are very close to zero, which leads us to choose  $d=3$  for analyzing cluster properties. The size of the clusters is set by choosing a covariance ellipsoid around each cluster centroid.

Figure 1

Figure 1 shows the clusters' complex three-dimensional (3-D) structure given semi-axes of the ellipsoid that correspond in length to 0.75 (heavy) and 1.25 (light) times the standard deviation in each direction. The names of the clusters are chosen based on the maps of the centroids, which will be discussed next. The arrows in Fig. 1 are projections of vectors that lie along preferred transitions paths between regimes and will be discussed in Section 4.

The anomaly maps of the 500-hPa streamfunction centroids shown in Fig. 1 are plotted in Fig. 2. Cluster  $AO^-$  (Fig. 2d) occupies a distinct region on the PDF ridge that stretches along PC-1, while clusters  $NAO^+$ ,  $NAO^-$  and  $AO^+$  are located around the global PDF maximum. Cluster  $NAO^+$  (Fig. 2a) is shifted away from the origin along PC-2, while clusters  $AO^+$  (Fig. 2c) and  $NAO^-$  (Fig. 2b) are shifted away from the PC-1 axis, in opposite directions with respect to PC-3.

Figure 2

Each of the regimes in Fig. 2 represents, roughly, one of the opposite phases of two spatial patterns. The maps in Figs. 2a and 2b capture the two extreme phases of the NAO, with the pattern in Fig. 2a completing a wavenumber-three pattern outside the Atlantic sector.

The maps in Figs. 2c and 2d have a large central anomaly that extends over the whole Arctic and a pronounced zonally symmetric component. The two maps thus have important features in common with the opposite phases of the AO (Thompson and Wallace 1998) and with Mo and Ghil’s (1988) North–South seesaw, while Fig. 2d also exhibits a substantial wavenumber-four component.

We denoted these four regimes, therefore, by  $NAO^+$  (panel a) and  $NAO^-$  (panel b),  $AO^+$  (panel c) and  $AO^-$  (panel d). The spatial patterns in Figure 2 resemble well four of the five clusters found by D’Andrea and Vautard (2001) in the QG3 model, by using the  $k$ -means method. We recall that  $NAO^+$  and  $NAO^-$  correspond to the zonal and blocked phases of the jet in the western North Atlantic, while  $AO^+$  and  $AO^-$  are composites of hemispherically high-index and low-index flow (in the sense used by J. Namias, C.-G. Rossby and H. Willet in the 1950s). The lack of symmetry between  $NAO^+$  and  $NAO^-$ , as well as between  $AO^+$  and  $AO^-$ , points to the potentially nonlinear origin of these regimes.

## 4 Markov chain of transitions

### *a. Transition probability matrix*

Given the clustering results of section 3, we proceed now to the main part of this study, namely investigating in detail the Markov chain of transitions between the four regimes. In a  $d$ -dimensional subspace of the model’s phase space, each weather regime is defined by the ellipsoid of covariance around the centroid, whose semi-axes equal the corresponding singular values, that is, the square roots of the eigenvalues of the covariance matrix of each Gaussian component (or a fixed multiple thereof; see Fig. 1). A data point is assigned to a weather regime if it lies within the corresponding ellipsoid. If a data point belongs to several ellipsoids, we assign it to a cluster according to the maximum probability value found from

the mixture model. We can vary the size of all four ellipsoids, and therefore the number of data points that belongs to each of the four clusters, by using the same scaling factor along the semi-axes of all four.

A regime event is defined as the number of consecutive points (days) along the model trajectory that fall within a given cluster (Mo and Ghil 1988; Kimoto and Ghil 1993b). Table 5 shows the number of distinct events in each regime and the total number of days spent in the regime for scaling factors of 0.75 and 1.25. A total number of about 25,000 days out of the entire run of 54,000 days belong to one of the large-size clusters ( $1.25\sigma$ ), while for the smaller clusters ( $0.75\sigma$ ) the total regime population is of about 7000 days.

Table 5

The distribution of residence times for each of the regimes is shown in Figure 3 (solid), together with associated significance curves (dashed); the latter correspond to one standard deviation of the residence time distribution within a population of 100 red-noise surrogate data samples (following Dole and Gordon 1983). Each surrogate sample consists of three AR(1) time series that have the the same length, variance and lag-1 autocorrelation coefficient as the QG3 model’s three leading PCs; the surrogate’s regime residence time is determined by the time spent by the sample trajectory in the cluster ellipsoids of our mixture model.

Figure 3

The persistence distributions are exponential in nature, and are similar in length and frequency of occurrence to those obtained by Corti et al. (1997) for the blocking episodes. The negative slopes of the residence curves become larger (in absolute value) and more equal to each other as the cluster size decreases (compare the curves for  $0.75\sigma$ , labeled by squares, with those for  $1.25\sigma$ , labeled by diamonds). For the large-size clusters (diamonds), the low-index cluster  $AO^-$  (Fig. 3d), albeit of relatively small total size (see Table 5), is visibly more persistent than the rest, while the sectorially zonal cluster  $NAO^+$  (Fig. 3a) is visibly less persistent. The zonal  $NAO^+$  regime is clearly less persistent than the corresponding

AR(1) process and the blocked  $NAO^-$  is slightly more persistent (although the difference is significant at larger durations only for  $0.75\sigma$ ), while  $AO^+$  and  $AO^-$  cannot be said to be significantly different from the AR(1) process.

Table 6

Table 6 shows transition probabilities between the clusters using the sequence of regime events along the trajectory. Note that when a trajectory exits a particular cluster, defined by the mixture modeling approach (as in Fig. 1), it may cross a "fuzzy" region of phase space, populated by data points that are not classified, before it ends up inside another cluster or the same one. Self-transitions are also counted, in addition to those that lead to another cluster, for computing transition probabilities between clusters.

Monte-Carlo simulation was applied to provide a statistical significance test for the elements of the transition matrix, following Vautard et al. (1990). The test is designed to take into account the difference in size between regimes and uses random shuffling of the sequence of regime events in the model simulation, subject to the constraint of the number of events in each regime being fixed and equal to the one in Table 5. The transition probabilities between regimes that are higher or lower than the Monte Carlo result at the 95% level appear in Table 6 in bold or italics, respectively. The results are similar (not shown) when only regime events that last for 3 days or longer have been considered. Note that each row in the table sums to unity, for all three cluster sizes being reported ( $0.75\sigma$ ,  $1.00\sigma$ , and  $1.25\sigma$ ).

The transition probabilities and their significance are fairly similar for the small and large clusters. The fact that there are more reentries for smaller-size clusters is entirely expected, since events of a given length are more likely to be erroneously "chopped up" into two or more events that belong to the same cluster, when its size is smaller; this finding merely suggests, therefore, that  $1.25\sigma$  is a somewhat better choice of scaling factor than  $0.75\sigma$  or  $1.00\sigma$ . All but one of the transitions were found to be significantly different from a random

shuffle for the largest clusters. The  $AO^-$  regime has a higher reinjection rate than the other three regimes, independently of scaling factor. By the previous reasoning about reentries and cluster size, this scale independence of its higher reinjection rate agrees with  $AO^-$  having the highest persistence (see Fig. 3d).

Taking the highest transition probability, excluding reentries, in every row, we obtain the preferential cycle of transitions:  $NAO^+ \rightarrow AO^+ \rightarrow NAO^- \rightarrow NAO^+$ ; the only disagreement between the estimates obtained with different scaling factors for this cycle is for the leg  $NAO^- \rightarrow NAO^+$  and so we have selected the transition for which all three estimates agree. A second cycle that is apparent only for  $1.0\sigma$  and  $1.25\sigma$  is  $AO^+ \leftrightarrow NAO^+$ . Transitions from each of the three regimes that have a small or negative PC-1 component to  $AO^-$  are unlikely by themselves but, taken together, they obviously add up to the low-index hemispheric regime  $AO^-$  being reachable from the higher-index part of the phase space. Direct transitions between  $AO^-$  and  $AO^+$  are very unlikely for all cluster sizes considered.

It is clear from this examination of the transition probability matrix that the model's LFV is quite nonlinear, with direct transition from the zonal to the blocked phase of the NAO,  $NAO^+$  to  $NAO^-$ , as well as between the high- and low-index phases of the AO,  $AO^+$  to  $AO^-$  or vice-versa, being quite unlikely. This agrees with the conclusions drawn from such transition matrices for NH observations by Mo and Ghil (1988) and Kimoto and Ghil (1993b). Given the model's degree of realism, on the one hand, and much greater availability of data points, on the other, we are thus motivated to explore certain details of its trajectory in phase space.

#### *b. Preferred transition paths*

To do so, we compute the exit angle from its regime for each events. When the model trajectory exits a cluster, we determine the phase space coordinates  $(x,y,z)$  of the exit point,

which is defined as the mid-point between two consecutive trajectory points that lie on the opposite sides of the cluster boundary. The exit vector is then defined to point from the cluster centroid to the exit point. In the 3-D subspace spanned by EOFs 1, 2, and 3, with coordinates  $(x, y, z)$ , each exit vector is uniquely defined by two angles:  $\tan \phi = y/x$ ,  $0 < \phi < 2\pi$ , and  $\tan \theta = z/(x^2 + y^2)$ ,  $-\pi/2 < \theta < \pi/2$ .

We then compute two-dimensional (2-D) PDF distributions of the exit angles in the  $(\phi, \theta)$  coordinates for all of the regime events using a Gaussian kernel estimator (Silverman 1986). This estimator approximates a PDF by assigning a localized kernel density function of a given shape (Gaussian in our case) to each data point. The PDF estimate at any point in phase space is then given by the sum of these kernel density functions. We use the data-adaptive version of the kernel estimator (Kimoto and Ghil 1993a) and modify it to account for the periodic nature of the PDF in the  $\phi$  direction. The PDFs so obtained are too noisy for smaller-size clusters ( $0.75\sigma$  and  $1.00\sigma$ ), due to the small number of regime events. We show therefore in Fig. 4 only the exit-angle PDFs for the largest-size clusters ( $1.25\sigma$ ), a choice that is also consistent with the earlier argument in the previous subsection on this size being less subject to reentries. The global PDF maxima in Fig. 4 are indicated by filled triangles, while open triangles mark strong secondary maxima, asterisks correspond to the straight line that connects the two cluster centroids in question, and filled circles correspond to the transition vectors determined by the transition patterns (see below).

Inspection of Fig. 4 demonstrates that most of the highly significant transitions (see again Table 6) occur along one or two narrow solid angles in phase space. For example, the  $NAO^+$  to  $AO^+$  and  $NAO^-$  to  $NAO^+$  transitions (Figs. 4a,b) have a narrow double peak in the PDF distribution, while the  $NAO^-$  to  $AO^+$  transition (Fig. 4c) has a single narrow maximum. The transitions from  $AO^+$  to  $NAO^-$  and  $AO^+$  to  $NAO^+$  (Figs. 4d,e), while still highly significant, are not quite as sharply confined in this angular PDF. As expected

Figure 4

from the conclusions of section 4a, the preferred directions of transition lean away from the straight line that connects the cluster centroids. To examine more closely the possible connections between a model’s nonlinear dynamics and its preferred regime transition angles, we study these connections for the Lorenz (1963a) system in Appendix A.

From the example of the Lorenz model we conclude that the observed maxima in the PDF distributions of the regime exit angles in our QG3 model are likely to be determined by the dynamical properties of the underlying nonlinear system of equations. These properties include the linearly stable and unstable directions of the steady states, as well as genuinely nonlinear, finite-amplitude behavior away from these steady states. Unlike in the Lorenz model, a distinct feature of both the  $NAO^+ \rightarrow AO^+$  and  $NAO^- \rightarrow NAO^+$  transitions is the appearance of a double peak in the exit-angle PDFs (see Figs. 4a,b). Such fine details of the regime transitions are being further examined in a nonlinear, stochastically forced system of 15 ordinary differential equations that represents a low-order version of the QG3 model (D. Kondrashov, S. Kravtsov, K. Ide, and M. Ghil, in preparation).

The spatial patterns associated with the preferred transition paths are shown in Fig. 5. These patterns correspond to "second-order anomalies," that is to deviations from the cluster centroids in a preferred direction of transition. For any transition in Fig. 4 we compute a composite anomaly map of the exit points from the regime, and then subtract from it the anomaly map of the cluster centroid. The patterns so obtained are robust with respect to cluster size and the length of the simulated data set (not shown). These patterns are significantly different from those obtained by just taking the differences between the cluster centroids: compare the position of the filled circles with that of the asterisks in Figs. 4a–d. Also, the patterns for transitions back and forth between a pair of clusters are strongly anticorrelated but the correlation is significantly distinct from  $-1.0$ : thus for  $NAO^- \leftrightarrow AO^+$  it is  $-0.53$ , while for  $AO^+ \leftrightarrow NAO^+$  it is  $-0.62$ .

Figure 5

The transitions between  $NAO^+$  and  $AO^+$  and back (Figs. 5a,e) exhibit both a strong SW–NE-oriented dipole, extending over much of the Central North Pacific and Gulf of Alaska. Those between  $NAO^-$  and  $AO^+$  share a strong, N–S-oriented dipole (with opposite polarities, obviously, in panels c and d) but the transition in Fig. 5c also has a strong feature in the Central North Pacific, which Fig. 5d lacks. Finally, the  $NAO^- \rightarrow NAO^+$  transition (Fig. 5b) is characterized by a wave train across North America that suggests a downstream influence of the Rockies (Kalnay-Rivas and Merkin 1983).

The projection of these transition patterns on the three leading EOFs determines the preferred transition vectors indicated by arrows in Fig. 1; the magnitude of these vectors, though, is not related to velocity in phase space and thus gives no indication on the rapidity of the corresponding regime break. The relative direction of the arrows is consistent with the correlation coefficients between the patterns: for example the arrows that correspond to the back-and-forth transitions between the pairs  $NAO^- \leftrightarrow AO^+$  and  $AO^+ \leftrightarrow NAO^+$  are almost at right angles to each other in Fig. 1a, in both cases. Note that this agreement is not self-evident, since the pattern correlations are computed in the full physical space, while the arrows correspond to projections onto a low-dimensional subspace.

## 5 Intraseasonal oscillations

In sections 3 and 4, we have provided an episodic description of the model’s LFV, based on the Markov chain of transitions between its four regimes. Given the overall realism of the model’s LFV, it seems appropriate to complement this description, if possible, with an oscillatory one that uses unstable limit cycles to describe the preferred trajectories in the model’s phase space.

Advanced spectral methods (Ghil et al. 2002) permit the statistically reliable identification and description of the least unstable limit cycles (see, in particular, Fig. 1

there). We apply singular spectrum analysis (SSA) to study the model’s intraseasonal oscillations and attempt to connect them with the statistically significant closed cycle  $NAO^+ \rightarrow AO^+ \rightarrow NAO^- \rightarrow NAO^+$  in regime transitions. Multi-channel SSA (M-SSA) generalizes single-channel SSA to extract oscillatory modes of variability from a multivariate time series and is especially useful in the study of amplitude- and phase-modulated signals. Keppenne and Ghil (1993) and Plaut and Vautard (1994), among others, have applied M-SSA to isolate oscillatory components in observations of atmospheric LFV.

We apply M-SSA to the three leading PCs of the 500-hPa streamfunction anomalies of our model integration,  $\{X_l(t) : t = 1, \dots, N\}$ , with  $N=54,000$ . The choice of three channels,  $1 \leq l \leq L = 3$ , is based on the conclusions of section 3, where we found  $d=3$  to be the optimal dimension of the subspace in which to compare the results of our two clustering methods. The notation here follows Ghil et al. (2002; see, in particular, Table 1 there) and we use the trajectory matrix approach of Broomhead and King (1986a,b), to compute the lag-covariance matrix.

The multi-channel trajectory matrix  $\tilde{\mathbf{X}}$  is formed by first augmenting each channel  $X_l(t)$  of the vector time series  $\mathbf{X}(t)$  with  $M$  lagged copies of itself, to yield  $\tilde{\mathbf{X}}_l(t)$ . The full augmented trajectory matrix is then given by:

$$\tilde{\mathbf{X}} = \left( \tilde{\mathbf{X}}_1, \tilde{\mathbf{X}}_2, \dots, \tilde{\mathbf{X}}_L \right). \quad (2)$$

The window width  $M$  determines the range of oscillation periods to be detected; to encompass the full range of intraseasonal oscillations, we have used values of  $M$  up to and including 100 days. The grand lag-covariance matrix  $\tilde{\mathbf{C}}_{\mathbf{X}}$  is given by

$$\tilde{\mathbf{C}}_{\mathbf{X}} = \frac{1}{N'} \tilde{\mathbf{X}}^t \tilde{\mathbf{X}}, \quad (3)$$

where  $N' = N - M + 1$ .

The eigenvectors of the matrix  $\tilde{\mathbf{C}}_{\mathbf{X}}$  are known as space-time EOFs or ST-EOFs. The associated space-time PCs (ST-PCs) are single-channel time series that are computed by projecting  $\tilde{\mathbf{X}}$  onto the ST-EOFs. M-SSA identifies an oscillation in the multivariate time series when two consecutive eigenvalues of  $\tilde{\mathbf{C}}_{\mathbf{X}}$  (ordered by size) are nearly equal, the corresponding ST-EOFs are periodic, with the same period and in quadrature, and the associated ST-PCs are in quadrature as well. Following Allen and Robertson (1996) we apply, in addition to the criteria above, a Monte-Carlo test to ascertain the statistical significance of the oscillations detected by M-SSA.

Figure 6 shows the eigenvalues obtained by M-SSA with a window width of  $M = 100$  days; these equal the variances associated with the corresponding eigenmode. The two arrows in Fig. 6 point to the M-SSA modes 8–9 and 15–16, which form two significant oscillatory pairs, with a period of 37 and 19 days, respectively. In addition, these pairs pass the lag-correlation test (not shown) of Plaut and Vautard (1994): on both sides of lag 0, the two successive extrema of the lag-autocorrelation of the corresponding ST-PCs exceed 0.5 in absolute value. The reconstructed components (RCs) of the 8–9 and 15–16 pairs describe the unstable limit cycle associated with the corresponding pair in the reduced phase space.

Figure 6

We analyze the behavior of the oscillation by using composite maps keyed to the phases of the oscillation, as in Plaut and Vautard (1994). Figures 7a–d show four successive, equally populated composites that correspond to one half-cycle of the 37-day oscillation. The cycle of regime transitions  $NAO^+ \rightarrow AO^+ \rightarrow NAO^-$  is easily identified. After passing through the  $NAO^+$  (Fig. 7a) and  $AO^+$  (Fig. 7b) phases, however, the next phase of the oscillation resembles the Pacific–North-American ( $PNA$ ) pattern (Fig. 7c), before reaching the  $NAO^-$  phase (Fig. 7d).

Figure 7

There is a certain similarity between some phases of this oscillation and certain phases

of the westward-propagating Branstator (1987)–Kushnir (1987) wave, as documented also by Dickey et al. (1991), Ghil and Mo (1991), and Plaut and Vautard (1994); see especially Fig. 5 of Branstator (1987). There are also marked differences, however, such as the 37-day period here vs. that wave’s period of 23–25 days, and the very pronounced features of Fig. 7 in the North-Atlantic–European sector. We constructed therefore a movie (not shown, but available upon request from the corresponding author; see also our web site <http://www.atmos.ucla.edu/tcd>), based on 100 composite maps of the cycle, rather than the eight composites for the full cycle used to construct Fig. 7.

The movie makes it clear that the 37-day cycle here is mainly a standing oscillation, with occasional northeastward propagation of certain features. In particular it shows strong interaction between the Rockies, on the one hand, and a low and a high that switch places in a counterclockwise fashion between lying upstream and downstream of this mountain range, on the other. The period and standing features of this oscillation, as well as its interaction with the Rockies, resemble certain characteristics of the oscillatory topographic instability of Ghil and associates (Legras and Ghil 1985; Ghil 1987; Ghil and Mo 1991; Ghil et al 1991; Ghil and Robertson 2002).

Phase composites of the 19-day oscillation (not shown) are almost identical to Figs. 7a–d. This similarity in spatial patterns, as well as the ratio between the periods of the oscillations being so close to 2, make one suspect that they are related as (sub)harmonics of each other. Following Plaut and Vautard (1994) and Koo et al. (2002), we calculated the histogram of simultaneous phase occurrences of the two oscillations. This calculation shows that they are not phase-locked to each other.

Another possible connection between the episodic and oscillatory description of preferred trajectories in phase space is to determine the average time taken by the model to complete the Markov-chain cycle  $NAO^+ \rightarrow AO^+ \rightarrow NAO^- \rightarrow NAO^+$ . As suggested by Fig. 1 in

Ghil et al. (2002), we computed this average only for those segments of trajectory that actually complete such a cycle by starting in one of these three regimes, passing through the other two in succession, and returning to the starting regime. The average cycle period computed in this way equals approximately 19 days, which is consistent with the shorter period of oscillation detected by M-SSA.

Legras and Ghil (1985) highlighted the slowing down of trajectories near unstable equilibria. Following this suggestion, Vautard (1990) used trajectory speeds as clustering criteria in observational data, while Mukougawa (1988) and Vautard and Legras (1988) used them in intermediate models of lesser complexity than the present ones; see also Table 1 in Ghil and Robertson (2002). We want to know, therefore, whether there is a systematic connection between any of the regimes and the slow phases of the oscillations described by M-SSA.

To investigate this connection, if any, we compute the velocity in the reduced phase space spanned by the three leading EOFs, along the trajectory of RCs 8–9, during a particular 100-day long oscillatory spell. The velocity components are obtained by central-differencing the time series for each of the three channels in the RCs. Figures 8a–c display the three velocity components, and Fig. 8d presents the speed. Likewise, the three velocity components and the speed for a 150-day long oscillatory spell with a 19-day period (RCs 15–16) are plotted in Figs. 8e–h.

Each velocity component is highly periodic, with the periods of 37 and 19 days, respectively, and the speed goes through phases of significant acceleration and deceleration. The period of the speed (Figs. 8d,h) seems to equal half the period of the velocity components, in the case of both unstable orbits. Alternate minima of the speed are associated with  $NAO^+$  and  $AO^+$ , for the 39-day cycle (Fig. 8d), as well as for the 19-day cycle (Fig. 8h).

Figure 8a-h

## 6 Concluding remarks

### *a. Summary*

We have examined the low-frequency variability (LFV) of the NH midlatitude atmosphere in the intermediate-complexity QG3 model of Marshall and Molteni (1993). The model is based on the QG equations for the conservation of potential vorticity and it has 3 levels in the vertical and T21 truncation in the horizontal (see section 2.) Using fairly realistic topography, land-sea contrast and residual forcing (see Corti et al. 1997), it produces respectable climatology and LFV.

#### 1) MARKOV CHAIN

We analyzed a 54,000-day long perpetual-winter integration of this model from the point of view of coarse-graining its phase space (Ghil 1987; Haines 1994; Ghil and Robertson 2002). The first step in this approach is to verify the presence of clusters in the dataset that corresponds to multiple weather regimes. These represent, in principle, regions of higher probability density function (PDF) on the model's attractor.

Using both the  $k$ -means method of Michelangeli et al. (1995) and the Gaussian mixture modeling of Smyth et al. (1999), and optimizing the result with respect to both methods (see Tables 1–4 here and Robertson and Ghil 1999), we obtained four NH clusters (Fig. 1) in the subspace of the four leading EOFs of the simulation's 500-hPa streamfunction field. The projections of the cluster centroids of the fourth and subsequent EOFs are very small and so the remainder of the analysis was carried out in a 3-D subspace (see Fig. 1).

The four clusters (see Fig. 2) are  $NAO^+$  and  $NAO^-$ , that is the zonal and blocked phases of the North Atlantic Oscillation (NAO), and  $AO^+$  and  $AO^-$ , that is the high- and low-index phases of the Arctic Oscillation (AO). These four regimes are not identical to but

in fairly good conceptual agreement with the observational results of Cheng and Wallace (1993), using hierarchical clustering, and those of Smyth et al. (1999), using a Gaussian mixture model for a slightly different NH dataset.

As discussed by Smyth et al. (1999) and Ghil and Robertson (2002), the four regimes that are best supported by synoptic experience, as well as statistical analysis of the upper-air data for the past half-century, are the zonal and blocked phases of westerly flow in the Atlantic–Eurasian and Pacific–North-American (PNA) sector, respectively. Seeing the PNA-sector patterns replaced in our classification by the hemispheric  $AO^+$  and  $AO^-$  ones is thus not too surprising: the latter two overlap largely in the Atlantic–Eurasian sector with  $NAO^+$  and  $NAO^-$ , respectively, from which they differ mostly by very strong centers of action in the PNA sector (see again Fig. 2).

The second step in the multiple-regime approach to LFV is to determine the Markov chain of transitions between regimes (Ghil 1987; Mo and Ghil 1988; Molteni et al. 1990; Kimoto and Ghil 1993b). In the language of dynamical systems theory, this corresponds to a particular representation of the “skeleton of the attractor,” which we take here to mean its most interesting and robust part.

To get the most reliable results for the transition probabilities from this long run, we used ellipsoidal clusters based on the Gaussian mixture model that had semi-axes ranging from  $0.75\sigma$  to  $1.25\sigma$ , with  $\sigma$  the variance in the corresponding principal direction (see Fig. 1 and Tables 5 and 6). Transitions were evaluated for significance with respect to statistical testing for fixed-size ellipsoids at the 95% level, as well as by comparing results obtained with different-size clusters. Excepting self-transitions, we found five transitions to be highly significant (see Table 6):  $NAO^+ \rightarrow AO^+$ ,  $NAO^- \rightarrow NAO^+$ ,  $AO^+ \rightarrow NAO^-$ ,  $AO^+ \rightarrow NAO^+$ , and  $NAO^- \rightarrow AO^+$ ; the first three were significant independently of cluster size, the last two only for larger clusters ( $1.25\sigma$ ).

These five significant transitions can be organized into two cycles. The first one,  $NAO^+ \rightarrow AO^+ \rightarrow NAO^- \rightarrow NAO^+$ , is significant at the 95% level, independently of cluster size. The second one,  $AO^+ \leftrightarrow NAO^+$  is only so for the larger-size clusters. It is remarkable that direct transitions between the opposite phases of the AO are significantly unlikely, at the 95% level, independently of cluster size. Likewise a direct transition from the zonal  $NAO^+$  to the blocked  $NAO^-$  is quite unlikely (see again Table 6). As previously argued by Mo and Ghil (1988) and Kimoto and Ghil (1993b), based on observational data, the present model results strongly support the nonlinear origin of these well-established NH regimes.

The third step in our coarse-graining approach had only been suggested in previous work (Ghil 1987; Ghil and Childress 1987, Sec. 6.4). This step consists in examining whether there are preferential directions in which the system's trajectory in phase space leaves the regimes and it has been carried out here for the first time, to the best of our knowledge.

We performed this step in two different ways. First we computed, in the 3-D subspace spanned by the model's three leading EOFs, the exit PDF on the unit sphere around each regime centroid (shown in Fig. 4 for the larger-size clusters). The solid-angle PDFs for all but two significant transitions exhibit one ( $NAO^- \rightarrow AO^+$ ) or two ( $NAO^+ \rightarrow AO^+$  and  $NAO^- \rightarrow NAO^+$ ) sharp peaks; the single peak for  $AO^+ \rightarrow NAO^-$  and the double one for  $AO^+ \rightarrow NAO^+$  are somewhat broader and thus the PDF maxima, while still present, are less pronounced.

Second, we computed full-map composites of all the regime breaks associated with the five significant transitions. To be included in such a composite, the anomaly map has to be the midpoint between a data point on the full phase-space trajectory that has just left a cluster and the preceding one, just inside the cluster. The difference between this composite exit anomaly and that of the cluster centroid from which exit occurred is shown, for each significant transition, in Fig. 5. It is also projected on the three leading EOFs and then on

the unit sphere around each cluster centroid. The results are shown as filled circles in Figs. 4a–e.

For each panel in Fig. 4 we have thus to compare three points: the asterisk that shows the direction of the straight line passing through the two regime centroids involved in the transition, the filled triangle that indicates the global maximum of the exit-angle PDF, and the filled circle, as just explained. The difference in locations between the filled circle and the filled triangle corresponds to the fact that the former is computed using only the values of PCs 1–3 of each map, while the latter is based on the actual map (including, as it were, all PCs). This difference is only sizable for Fig. 4a.

Clearly, in the case of the exit-angle PDFs with a single sharp peak (Fig. 4c) the filled triangle marks this peak. For the double-peaked PDFs the preferred mean exit angle (filled circle) lies roughly between the two peaks (Figs. 4b,e). Only for the transition  $AO^+ \rightarrow NAO^+$  (Fig. 4e) does the straight line that passes through the two centroids (asterisk) lie close to the preferred mean exit angle (filled triangle or filled circle); see also Figs. 1a,b. It follows that the actual preferred paths for transitions between pairs of clusters lean overwhelmingly away from the line segment that unites the corresponding pair of centroids.

## 2) INTRASEASONAL OSCILLATIONS

A complementary way of describing the skeleton of our model’s attractor is by using the least-unstable periodic orbits (Ott et al. 1994, and references therein). We carried out multi-channel SSA (M-SSA) of the 54,000-day long trajectory (Plaut and Vautard 1994; Ghil et al. 2002) in the same subspace spanned by the three leading EOFs as for the Markov chain. Two pairs of oscillatory modes are statistically significant at the 95% level (Fig. 6); they have periods of 37 days (modes 8–9) and 19 days (modes 15–16). The spatial patterns

associated with a half-cycle of the 37-day oscillation are shown in Fig. 7; they are  $NAO^+ \rightarrow AO^+ \rightarrow PNA \rightarrow NAO^-$ . The Markov-chain cycle  $NAO^+ \rightarrow AO^+ \rightarrow NAO^- \rightarrow NAO^+$  thus appears embedded in the 37-day oscillation.

In fact, the average time taken by all the trajectory segments that complete the above cycle of three residence times in  $NAO^+$ ,  $AO^+$ , and  $NAO^-$ , as well as the three transitions indicated, equals about 19 days. The composite patterns for the 19-day oscillation resemble very well those of the Fig. 7, but the two oscillations do not seem to be phase locked.

The spatio-temporal patterns of the oscillations present certain similarities with the Branstator (1987)–Kushnir (1987) wave, on the one hand, and the oscillatory topographic instability of Ghil and associates (Ghil 1987; Ghil and Robertson 2002, and further references therein), on the other. A closer evaluation of these similarities, as well as of the differences, goes beyond the purpose of the present paper.

#### *b. Discussion*

The preferred transition paths between the two regimes found in a stochastically forced Lorenz (1963a) model (see Figs. 9 and 10) also point away from the line segment uniting the two centroids. In this simple case, the dynamic cause of this statistical result is well known: it is associated with the geometry of the unstable and stable manifolds of the original, deterministic model version’s unstable fixed points (Guckenheimer and Holmes 1983; Ghil and Childress 1987, Sec. 5.4) and with the fact that the deformation of these manifolds, as model parameters change, leads to the existence of hetero- and homoclinic “explosions” (Sparrow 1983) that generate its deterministic chaos. The stochastic forcing (Sutera 1980) merely plays the role of the small-scale, high-frequency components of the QG3 model and smears out the PDF associated with the deterministic Lorenz model’s chaotic behavior.

Hetero- and homoclinic orbits are well understood to play a major role in the nonlinear

behavior of dynamical systems in general, in spite of their elusiveness (Wiggins 1988). A homoclinic orbit arises when a fixed point's unstable manifold returns as its stable manifold. A heteroclinic connection involves the unstable manifold of a fixed point becoming the stable manifold of another fixed point. The importance of such orbits in the irregular behavior of atmospheric and oceanic models, and maybe of the actual atmosphere and oceans, has recently been discussed more widely. We sketch, therefore, a brief history of these applications and how it might relate to the results of this paper.

Lorenz (1963b) was the first, to the best of our knowledge, to mention the potential role of a heteroclinic orbit in transition to chaos for an atmospheric model. Ghil and Childress (1987, Secs. 5.3 and 5.5) discussed at length this role in connection with the Shilnikov (1965) "route to chaos." These authors also discussed, at some length, the role of unstable equilibria and a homoclinic orbit (see Fig. 6.12 and Sec. 6.4 there) in the genesis of regimes, as well as in their persistence, slow onset and rapid break. Both hetero- and homoclinic orbits are hard to compute exactly, because of their existence at isolated parameter values only. Still, they can strongly influence the behavior of the system at neighboring parameter values. A simple illustration is given in Ghil and Ghildress (1987; Fig. 12.10 and Sec. 12.2) for an oscillatory paleoclimate model.

Kimoto and Ghil (1993b) and Weeks et al. (1997) mentioned the possible role of a heteroclinic orbit in giving rise to regime transitions. Hetero- and homoclinic orbits were shown to play an important role in the interannual and interdecadal LFV of the midlatitude ocean's wind-driven circulation (Meacham 2000; Chang et al. 2001; Nadiga and Luce 2001; Simmonet et al 2003a,b). Crommelin (2002, 2003) explored in detail the role of such orbits in a low-order and an intermediate-order model of the extratropical atmosphere, respectively.

It is plausible that the statistically significant transitions between our model's four regimes are related to the presence, at nearby parameter values, of heteroclinic connec-

tions between unstable fixed points that lie near the cluster centroids. This conjecture is supported by the results of D’Andrea and Vautard (2001) and D’Andrea (2002), who found a good correspondence between their low-order model’s quasi-stationary states and the QG3 model’s regimes. The presence of heteroclinic connections is especially likely in the case of the transitions that lean quite noticeably away from the straight-line segments between pairs of centroids. Work in progress (D. Kondrashov, S. Kravtsov, K. Ide, and M. Ghil, in preparation), using a lower-order, stochastically forced model, is pursuing further the possible connections between preferred transitions and nonlinear dynamics in the QG3 model.

The model’s closed Markov chain cycle and its 37-day oscillatory mode both exhibit composite 500-hPa maps that resemble the  $NAO^+$ ,  $AO^+$ , and  $NAO^-$  spatial patterns in this order. This strong similarity is another illustration of the interesting, but elusive, relationship between the episodic, multiple-regime description of atmospheric LFV and the oscillatory one, based on intraseasonal oscillations (Kimoto and Ghil 1993b; Plaut and Vautard 1994; Ghil and Robertson 2002; Koo et al. 2002). It is quite possible, although still to be confirmed (see the previous paragraph), that these three regimes, all of which lie in the  $PC-1 \leq 0$  half of the model’s phase space, are connected by heteroclinic orbits. Not all three of these need coexist at exactly the same set of parameter values; it suffices that the appropriate parameter values lie close to each other and to those that are most realistic for matching the model behavior to NH atmospheric LFV.

Last, but not least, the original motivation for undertaking this study was our interest in exploiting satellite data, including satellite images, for the early identification of regime breaks. The preferred transition patterns shown in Figs. 5a–e have synoptic features that are easily identifiable and can foretell an abrupt break in a given regime, while the day’s map lies still within a fairly small distance of that regime’s centroid. This identification might be done numerically, within the evolution of an operational forecast-analysis cycle that uses an

advanced numerical weather prediction model.

It might also be possible to identify these transition patterns by using directly advanced image processing methods on cloud imagery or other fields produced by satellite-based instruments, with or without the use of model assimilation of these fields. It is true that spatio-temporal LFV patterns captured in observational datasets only reflect a few tens of percent of the total variance of the data (Kimoto and Ghil 1993a,b; Brunet 1994). Still, advanced data mining and knowledge discovery tools from computer science and nonparametric statistics (Hand et al. 2001) can help extract this information from the high level of weather noise, due to its regularities in space or time.

## 7 Acknowledgments

We are grateful to Fabio D’Andrea for providing a code of the QG3 model and information on its performance. Andrew W. Robertson and Padhraic J. Smyth provided the codes for the  $k$ -means method and the Gaussian mixture model, respectively; it is a pleasure to thank them for the codes and their advice on using these. We also wish to thank Sergey Kravtsov and Ricardo Todling for helpful discussions, and Daan Crommelin for sharing preprints of his recent work. Gilbert Brunet and an anonymous reviewer provided constructive comments on a previous version of the paper. Our study was supported by NASA grant NAG5-9294 and NSF grant ATM00-8213. This is publication No. 5825 of UCLA’s Institute of Geophysics and Planetary Physics.

## Appendix A. Regime Transition Angles in the Lorenz Model

The Lorenz (1963a) system of three coupled, nonlinear, ordinary differential equations is obtained by spectral truncation of the Boussinesq equations for 2-D Rayleigh-Bénard con-

vection. We use this system subject to stochastic forcing, following Sutera (1980):

$$\dot{X} = -sX + sY + \epsilon, \tag{A.1a}$$

$$\dot{Y} = -XZ + rX - Y + \epsilon, \tag{A.1b}$$

$$\dot{Z} = XY - bZ + \epsilon, \tag{A.1c}$$

where  $\epsilon$  is a white-noise process (see below). In the original Lorenz system (for  $\epsilon=0$ ) the parameters  $s=10$ ,  $r=28$  and  $b=8/3$  lead to chaotic internal variability caused by the system's instabilities and nonlinearity (see also Guckenheimer and Holmes 1983; Ghil and Ghildress 1987).

There are two unstable steady states at  $W_1 = (6\sqrt{2}, 6\sqrt{2}, 27)$  and  $W_2 = (-6\sqrt{2}, -6\sqrt{2}, 27)$ . Each of these states is stable in one direction, and unstable in the other two. The third steady state  $W_0 = (0, 0, 0)$  is stable along the  $Z$ -axis and in one additional direction, and unstable in the third. Due to the oscillatory instability of  $W_1$  and  $W_2$ , the trajectories spiral out around either one of these two points with increasing amplitude. As each such spiral reaches a threshold value imposed by the system's quadratic nonlinearity, it leaves the neighborhood of the unstable point it started from, crosses near the axis of mirror symmetry given by  $X = Y = 0$ , and lands near the opposite unstable point. This behavior then repeats itself in the opposite direction so that the trajectory switches irregularly from the neighborhood of  $W_1$  to that of  $W_2$  and back. These repetitions occur irregularly in time and give rise to two regimes in the Lorenz system, each of which consists of the spiral segments of orbit around  $W_1$  and  $W_2$ , respectively.

To make the analogy with the QG3 model more realistic, we stochastically force the Lorenz system with a white-noise term  $\epsilon = \epsilon(t)$ , having variance  $\sigma_\epsilon^2 = 2$ . This forcing provides a crude approximation of the effect of the smaller scales and higher frequencies on

the LFV of the QG3 model and the atmosphere. More precisely, we transform the system (A.1) into its proper stochastic differential form

$$d\mathbf{X} = \mathbf{f}(\mathbf{X})dt + \sigma_\epsilon d\boldsymbol{\beta}, \quad (\text{A.2})$$

where  $\mathbf{X} = (X, Y, Z)^T$  and  $\mathbf{f}$  is the nonlinear, deterministic right-hand side of (A.1), while  $\boldsymbol{\beta}(t)$  is the appropriate Wiener process whose "derivative" is the white noise  $\epsilon(t)$ . We use an Euler scheme with a time step of 0.01 (Kloeden and Platen 1992) to obtain a long realization of the stochastic process governed by (A.2) for 50,000 time steps.

The strong non-Gaussian nature of the Lorenz attractor leads to a systematic bias towards a higher number of clusters when a cross-validated log-likelihood procedure is used (Hannachi and O'Neill 2001). Since we know already the true equations generating the data and the regimes in our system, we apply the mixture model with two clusters to the time series of  $(X, Y, Z)$ . In the original Lorenz system ( $\epsilon=0$ ) the trajectories are bound away from the points  $W_1$  and  $W_2$  at this value of  $s$ ,  $r$  and  $b$ . Stochastic forcing fills in these gaps, as seen in Figs. 9a, b of the mixture model's PDF, projected on the  $X$ - $Y$  and  $X$ - $Z$  planes, respectively. The arrows in Fig. 9 are projections of vectors that lie along preferred transition paths between regimes that are obtained by the same method as described in section 4.

Figure 9

The regime exit angles  $\phi$  and  $\theta$  and their PDF distributions for the Lorenz system's two clusters are computed with the same procedure as for the QG3 model, and the results are shown in Fig. 10. The locations of the two sharp maxima are explained by the orbit's crossing from one regime into the other in the vicinity of the  $Z$ -axis. When the orbit's projection on the  $X$ - $Y$  plane spirals out within one of the clusters, it approaches the origin along the stable direction of the  $W_0$  state; this direction does not coincide with the straight line that passes through  $W_1$  and  $W_2$ . The orbit then leaves the neighborhood of the origin along the unstable direction of the  $W_0$  state, thus entering the other cluster. The values of

Fig. 10

$\phi$  at the PDF maxima are therefore higher than the value that corresponds to the  $W_1 \rightarrow W_2$  line segment. The negative but small value of  $\theta$  at the PDF maximum is caused by the orbit proceeding in the negative direction along the  $Z$ -axis while exiting either cluster.

Ideally, the symmetry of the dynamics about the  $Z$ -axis should lead to the symmetry of the exit-angle PDF between the two regimes; this symmetry would imply that Figs. 10a and 10b should be identical, modulo a shift of  $\pi$  in the  $\phi$  direction. The length of the dataset here, however, has been chosen to match approximately the length of the QG3 model integration, in appropriate units. Therefore the mismatch between Figs. 10a and 10b gives an idea of the sampling-error effect in Figs. 4a–e.

The connection between the detailed geometry of regime transitions in the Lorenz model, as captured in Figs. 9 and 10, and the structure of the stable and unstable manifolds of the unstable fixed points  $W_0$ ,  $W_1$  and  $W_2$  should be apparent by inspecting Figs. 5.10 and 5.11 of Ghil and Ghildress (1987). Sparrow (1982) has investigated thoroughly the role of homoclinic and heteroclinic orbits that arise from these manifolds, given changes in the Lorenz (1963a) model's parameters  $s$ ,  $r$  and  $b$ , in generating the model's chaotic behavior.

## References

- Allen, M. R., and A. W. Robertson, 1996: Distinguishing modulated oscillations from coloured noise in multivariate datasets. *Clim. Dyn.*, **12**, 775–784.
- Branstator, G. W., 1987: A striking example of the atmosphere’s leading traveling pattern. *J. Atmos. Sci.*, **44**, 2310–2323.
- Broomhead, D. S., and G. P. King, 1986a: Extracting qualitative dynamics from experimental data. *Physica* **D20**, 217–236.
- Broomhead, D. S., and G. P. King, 1986b: On the qualitative analysis of experimental dynamical systems. In: Sarkar S. (ed.), *Nonlinear Phenomena and Chaos*. Adam Hilger, Bristol, pp. 113–144.
- Brunet, G., 1984: Empirical normal-mode analysis of atmospheric data. *J. Atmos. Sci.*, **51**, 932–952.
- Chang, K.-I., M. Ghil, K. Ide, and C.-C. A. Lai, 2001: Transition to aperiodic variability in a wind-driven double-gyre circulation model, *J. Phys. Oceanogr.*, **31**, 1260–1286.
- Cheng, X. H., and J. M. Wallace, 1993: Cluster-analysis of the northern-hemisphere winter-time 500-hPa height field spatial patterns, *J. Atmos. Sci.* **50**, 2674–2696.
- Corti, S., A. Giannini, S. Tibaldi, and F. Molteni, 1997: Patterns of low-frequency variability in a three-level quasi-geostrophic model, *Clim. Dyn.*, **13**, 883–904.
- Crommelin, D. T., 2002: Homoclinic dynamics: a scenario for atmospheric ultra-low-frequency variability, *J. Atmos. Sci.*, **59**, 1533–1549.
- , 2003: Regime transitions and heteroclinic connections in a barotropic atmosphere., *J. Atmos. Sci.*, in press.
- D’Andrea, F., and R. Vautard, 2001: Extratropical low-frequency variability as a low-dimensional problem. Part I: a simplified model, *Q. J. R. Meteorol. Soc.*, **127**, 1357–1374.
- , 2002: Extratropical low-frequency variability as a low-dimensional problem. Part II: stationarity and stability of large-scale equilibria, *Q. J. R. Meteorol. Soc.*, **128**, 1059–1073.
- Dickey, J. O., M. Ghil, and S. L. Marcus, 1991: Extratropical aspects of the 4050 day oscillation in length-of-day and atmospheric angular momentum, *J. Geophys. Res.*, **96**, 22643–22658.

- Dole, R. M., and N. D. Gordon, 1983: Persistent anomalies of the extratropical northern hemisphere wintertime circulation — geographical distribution and regional persistence characteristics, *Mon. Wea. Rev.*, **111**, 1567–1586.
- Ghil, M., 1987: Dynamics, statistics and predictability of planetary flow regimes, *Irreversible Phenomena and Dynamical Systems Analysis in the Geosciences*, C. Nicolis and G. Nicolis (Eds.), D. Reidel, Dordrecht/Boston/Lancaster, pp. 241–283.
- , and S. Childress, 1987: *Topics in Geophysical Fluid Dynamics: Atmospheric Dynamics, Dynamo Theory and Climate Dynamics*, Springer-Verlag, New York/Berlin/London/Paris/ Tokyo, 485 pp.
- , and K.-C. Mo, 1991: Intraseasonal oscillations in the global atmosphere. Part I: Northern Hemisphere and tropics, *J. Atmos. Sci.*, **48**, 752–779.
- , S. L., Marcus, J. O. Dickey, and C. L. Keppenne, 1991: *AAM the Movie*. NTSC videocassette AVC-91-063, Caltech/NASA Jet Propulsion Laboratory, Pasadena, CA 91109 [available also from MG upon request].
- , M., M. R. Allen, M. D. Dettinger, K. Ide, D. Kondrashov, M. E. Mann, A. W. Robertson, A. Saunders, Y. Tian, F. Varadi, and P. Yiou, 2002: Advanced spectral methods for climatic time series, *Rev. Geophys.*, **40**(1), pp. 3.1–3.41, 10.1029/2000GR000092.
- , and A. W. Robertson, 2002: "Waves" vs. "particles" in the atmosphere's phase space: A pathway to long-range forecasting? *Proc. Natl. Acad. Sci.*, **99** (Suppl. 1), 2493–2500.
- Guckenheimer, J., and P. Holmes, 1983: *Nonlinear Oscillations, Dynamical Systems, and Bifurcations of Vector Fields*, Springer-Verlag, New York/Berlin/London/Paris/ Tokyo, 453 pp.
- Haines, K., 1994: Low-frequency variability in atmospheric middle latitudes. *Surveys Geophys.*, **15**, 1–61.
- Hand D., H. Mannila, and P. Smyth, 2001: *Principles of Data Mining*. MIT Press, Cambridge, Mass., 546 pp.
- Hannachi, A., and A. O'Neill, 2001: Atmospheric multiple equilibria and non-Gaussian behaviour in model simulations. *Q. J. R. Meteorol. Soc.*, **127**, 939–958.
- Kalnay-Rivas, E., and L.-O. Merkin, 1983: A simple mechanism for blocking. *J. Atmos. Sci.*, **38**, 2077–2091.
- Keppenne, C. L., and M. Ghil, 1993: Adaptive filtering and prediction of noisy multivariate signals: An application to subannual variability in atmospheric angular momentum, *Intl. J. Bifurcation & Chaos*, **3**, 625–634.
- Kimoto, M., and M. Ghil, 1993a: Multiple flow regimes in the Northern Hemisphere winter. Part I: Methodology and hemispheric regimes. *J. Atmos. Sci.*, **50**, 2625–2643.

- , and M. Ghil, 1993b: Multiple flow regimes in the Northern Hemisphere winter. Part II: Sectorial regimes and preferred transitions, *J. Atmos. Sci.*, **50**, 2645–2673.
- Kloeden, P.E. and E. Platen, 1992: *Numerical Solution of Stochastic Differential Equations*. Springer-Verlag, Berlin/Heidelberg.
- Koo, S., and M. Ghil, 2002: Successive bifurcations in a simple model of atmospheric zonal-flow vacillation, *Chaos*, **12**, 300–309.
- , A. W. Robertson, and M. Ghil, 2002: Multiple regimes and low-frequency oscillations in the Southern Hemispheres zonal-mean flow, *J. Geophys. Res.*, **107**(D21), pp. **ACL 14.114.13**, 10.1029/2001JD001353.
- Kushnir, Y., 1987: Retrograding wintertime low-frequency disturbances over the North Pacific Ocean. *J. Atmos. Sci.*, **44**, 2727–2742.
- Legras, B., and M. Ghil, 1985: Persistent anomalies, blocking and variations in atmospheric predictability, *J. Atmos. Sci.*, **42**, 433–471.
- Lorenz, E. N., 1963a: Deterministic nonperiodic flow. *J. Atmos. Sci.*, **20**, 130–141.
- , 1963b: The mechanics of vacillation. *J. Atmos. Sci.*, **20**, 448–464.
- Marshall, J., and F. Molteni, 1993: Towards a dynamical understanding of planetary-scale flow regimes. *J. Atmos. Sci.*, **50**, 1792–1818.
- Meacham, S.P., 2000: Low-frequency variability in the wind-driven circulation. *J. Phys. Oceanogr.*, **30**, 269–293.
- Michelangeli, P.A., R. Vautard, and B. Legras, 1995: Weather regimes: Recurrence and quasi-stationarity. *J. Atmos. Sci.*, **52**, 1237–1256.
- Mo, K., and M. Ghil, 1987: Statistics and dynamics of persistent anomalies, *J. Atmos. Sci.*, **44**, 877–901.
- , and M. Ghil, 1988: Cluster analysis of multiple planetary flow regimes, *J. Geophys. Res.*, **93D**, 10927–10952.
- Molteni, F., and S. Corti, 1998: Long-term fluctuations in the statistical properties of low-frequency variability: Dynamical origin and predictability. *Q. J. R. Meteorol. Soc.* **124**, 495–526.
- , S. Tibaldi, and T.N. Palmer, 1990: Regimes in the wintertime circulation over northern extratropics. 1. observational evidence. *Q. J. R. Meteorol. Soc.*, **116**, 31–67.
- Mukougawa, H., 1988: A dynamical model of "quasi-stationary" states in large-scale atmospheric motions. *J. Atmos. Sci.*, **45**, 2868–2888.

- Nadiga, B.T., and B.P. Luce, 2001: Global bifurcation of Shilnikov type in a double-gyre ocean model. *J. Phys. Oceanogr.*, **31**, 2669–2690.
- Ott, E., T. Sauer, and J. A. Yorke (Eds.), 1994: *Coping with Chaos. Analysis of Chaotic Data and the Exploitation of Chaotic Systems*. J. Wiley & Sons, New York/Chichester/Brisbane/Toronto/Singapore, 418 pp.
- Plaut G., and R. Vautard, 1994: Spells of low-frequency oscillations and weather regimes in the northern hemisphere, *J. Atmos. Sci.*, **51**, 210–236.
- Robertson, A. W., and M. Ghil, 1999: Large-scale weather regimes and local climate over the western United States. *J. Climate*, **12**, 1796–1813.
- Shilnikov, L. P., 1965: A case of the existence of a denumerable set of periodic motions. *Sov. Math. Dokl.*, **6**, 163–166.
- Silverman, B.W. 1986: *Density Estimation for Statistics and Data Analysis*. Chapman and Hall, 175 pp.
- Simonnet, E., M. Ghil, K. Ide, R. Temam, and S. Wang, 2003a: Low-frequency variability in shallow-water models of the wind-driven ocean circulation. Part I: Steady-state solutions. *J. Phys. Oceanogr.*, **33**, 712–728.
- Simonnet, E., M. Ghil, K. Ide, R. Temam, and S. Wang, 2003b: Low-frequency variability in shallow-water models of the wind-driven ocean circulation. Part II: Time-dependent solutions. *J. Phys. Oceanogr.*, **33**, 729–752.
- Smyth, P., K. Ide, and M. Ghil, 1999: Multiple regimes in Northern Hemisphere height fields via mixture model clustering. *J. Atmos. Sci.*, **56**, 3704–3723.
- Sparrow, C., 1982: *The Lorenz Equations: Bifurcations, Chaos and Strange Attractors*. Springer-Verlag, New York, 269pp.
- Sutera, A., 1980: Stochastic perturbation of a pure convective motion, *J. Atmos. Sci.*, **37**, 246–249.
- Thompson, D. W., and J. M. Wallace, 1998: The Arctic Oscillation signature in the winter-time geopotential height and temperature fields. *Geophys. Res. Lett.*, **25**, 1297–1300.
- Vautard, R., 1990: Multiple weather regimes over the North Atlantic. Analysis of precursors and successors. *Mon. Wea. Rev.*, **118**, 2056–2081.
- , and B. Legras, 1988: On the source of low frequency variability. Part II: Nonlinear equilibration of weather regimes. *J. Atmos. Sci.*, **45**, 2845–2867.
- , K. C. Mo, and M. Ghil, 1990: Statistical significance test for transition matrices of atmospheric Markov chains, *J. Atmos. Sci.*, **47**, 1926–1931.

- Wallace, J.M., 2000: North Atlantic Oscillation/annular mode: Two paradigms - one phenomenon *Q. J. R. Meteorol. Soc.* **126**, 791–805.
- Weeks, E. R., Y. Tian, J. S. Urbach, K. Ide, H. L. Swinney, and M. Ghil, 1997: Transitions between blocked and zonal flows in a rotating annulus with topography. *Science*, **278**, 1598–1601.
- Wiggins, S., 1988: *Global Bifurcations and Chaos: Analytical Methods*, Springer-Verlag, New York.

## Tables

**Table 1.** Classifiability index of the  $k$ -means algorithm:  $k$  is the prescribed number of clusters, while  $d$  is the number of the EOFs retained for the analysis.

	$k=3$	$k=4$	$k=5$
$d=2$	1.000	0.973	1.000
$d=3$	1.000	1.000	1.000
$d=4$	1.000	1.000	0.819
$d=5$	1.000	1.000	0.807

**Table 2.** Cross-validated log-likelihood for 18,000 data points, using only the first third of the full dataset: the lower the absolute value of this score, the more likely the corresponding  $k$ -value is for a given  $d$ .

	$k=1$	$k=2$	$k=3$	$k=4$	$k=5$
$d=2$	-22770	-22296	-22255	-22248	-22245
$d=3$	-31839	-31314	-31274	-31233	-31233
$d=4$	-40445	-39889	-39836	-39815	-39821
$d=5$	-48342	-47737	-47682	-47681	-47687

**Table 3.** Cross-validated log-likelihood for the entire set of 54,000 data points.

	$k=1$	$k=2$	$k=3$	$k=4$	$k=5$
$d=2$	-67749	-66396	-66286	-66226	-66214
$d=3$	-94685	-93114	-92926	-92823	-92760
$d=4$	-120233	-118494	-118311	-118158	-118113

**Table 4.** Correlation coefficients between pairs of clusters given by the mixture model, on the one hand, and  $k$ -means clusters, on the other, when retaining  $k$  clusters: (a)  $k=3$ ; (b)  $k=4$ , and (c)  $k=5$ . In each case, correlations are given for the pairs identified by best visual match, and  $1 \leq n \leq k$ .

a)	$n=1$	$n=2$	$n=3$
$d=2$	0.999	0.995	0.993
$d=3$	0.996	0.995	0.993
$d=4$	0.996	0.994	0.994
$d=5$	0.992	0.990	0.986

b)	$n=1$	$n=2$	$n=3$	$n=4$
$d=2$	0.991	0.959	0.947	0.913
$d=3$	0.997	0.986	0.982	0.970
$d=4$	0.997	0.996	0.995	0.989
$d=5$	0.996	0.994	0.991	0.985

c)	$n=1$	$n=2$	$n=3$	$n=4$	$n=5$
$d=2$	0.993	0.993	0.980	0.969	0.954
$d=3$	0.994	0.990	0.925	0.919	0.628
$d=4$	0.999	0.998	0.996	0.979	0.949
$d=5$	0.999	0.997	0.993	0.990	0.882

**Table 5.** Regime statistics for different cluster sizes. The cluster size is determined by the scaling factor of the standard deviation  $\sigma$  along each semi-major axis.

Size		$NAO^+$	$NAO^-$	$AO^+$	$AO^-$	Total
$0.75\sigma$	Events	908	1137	1026	673	3744
	Days	1602	2030	1930	1322	6884
$1.25\sigma$	Events	1970	2375	2319	1665	8329
	Days	5248	6956	6740	5603	24547

**Table 6.** Transition probabilities estimated using the mixture model. Transitions that are significantly higher at the 95% level with respect to 10,000 random shuffles of the sequence of regime events are in bold, while entries that are italicized are significantly lower at the 95% level for the same test. The entries in the table are for clusters of size  $0.75\sigma$ ,  $1.0\sigma$  and  $1.25\sigma$ , in this order. Not all rows sum exactly to 1.00 because of round-off effects.

$0.75\sigma/1.00\sigma/1.25\sigma$	$NAO^+$	$NAO^-$	$AO^+$	$AO^-$
$NAO^+$	<b>0.33/0.29/0.25</b>	<i>0.27/0.23/0.21</i>	<b>0.34/0.41/0.44</b>	<i>0.06/0.07/0.10</i>
$NAO^-$	<b>0.26/0.27/0.26</b>	<b>0.32/0.28/0.25</b>	0.27/0.28/0.30	<i>0.15/0.17/0.19</i>
$AO^+$	0.24/ <b>0.29/0.29</b>	<b>0.38/0.39/0.40</b>	<b>0.31/0.27/0.25</b>	<i>0.07/0.05/0.06</i>
$AO^-$	<i>0.11/0.09/0.10</i>	<i>0.20/0.22/0.26</i>	<i>0.13/0.10/0.10</i>	<b>0.56/0.59/0.53</b>

## Figure captions

Fig. 1: Probability density function (PDF) of the QG3 model's 500-hPa streamfunction field, as estimated by the mixture model for  $d = 3$  and  $k = 4$ . The PDF is projected onto the plane spanned by (a) PC-1 and PC-2, and (b) PC-1 and PC-3; 20 contour levels are used. The heavy ellipses correspond to semi-axes equal to  $0.75\sigma$  in each principal direction, while the light ones correspond to  $1.25\sigma$ . Arrows indicate the preferred transition paths obtained in section 4b. The mixture model centroids have the following coordinates:  $NAO^+ = (-0.44, 0.75, -0.09)$ ,  $NAO^- = (-0.10, -0.31, -0.46)$ ,  $AO^+ = (-0.71, -0.23, 0.29)$ , and  $AO^- = (1.14, -0.03, 0.25)$ .

Fig. 2: Mixture model centroids for  $d = 3$  and  $k = 4$ , showing streamfunction anomaly maps at 500 hPa: a)  $NAO^+$ ; b)  $NAO^-$ ; c)  $AO^+$ ; and d)  $AO^-$ . Negative contours are dashed and land masses are shaded; twenty contour levels between maximum and minimum values are used, with the following intervals (in  $10^6 \text{ m}^2\text{s}^{-1}$ ): a) 1.1, b) 0.8, c) 0.8, and d) 1.1 .

Fig. 3: Distribution of cumulative residence time (solid lines) in the model's regimes for cluster sizes of  $0.75\sigma$  and  $1.25\sigma$ , where  $\sigma$  refers to the standard deviation of each regime, along each semi-major axis (omitting subscripts). Dashed lines correspond to one standard deviation, above and below the mean of the residence time distribution, within a population of 100 red-noise surrogate data samples (see text for details). Panels (a)–(d) correspond to the four regimes shown in Figs. 1 and 2.

Fig. 4: 2-D PDF of regime exit angles for the largest-size clusters: a)  $NAO^+ \rightarrow AO^+$ ; b)  $NAO^- \rightarrow AO^+$ ; c)  $NAO^- \rightarrow AO^+$ ; d)  $AO^+ \rightarrow NAO^-$ ; and e)  $AO^+ \rightarrow NAO^+$ . Asterisks correspond to the straight line that connects the two cluster centroids in question, filled circles correspond to the vectors determined by the composite transition

patterns in Fig. 5, and filled triangles correspond to global PDF maxima, while open triangles mark strong secondary maxima. The contour interval for all panels is equal to 0.2 in nondimensional units. For economy of space, the scaling along the abscissa ( $\phi$ -axis) is twice that along the ordinate ( $\theta$ -axis).

Fig. 5: Spatial transitions patterns: a)  $NAO^+ \rightarrow AO^+$ ; b)  $NAO^- \rightarrow AO^+$ ; c)  $NAO^- \rightarrow AO^+$ ; d)  $AO^+ \rightarrow NAO^-$ ; and e)  $AO^+ \rightarrow NAO^+$ . Ten contour levels are used between maximum and minimum values, with the following intervals (in  $10^6 \text{ m}^2\text{s}^{-1}$ ): a) 1.0, b) 1.3, c) 1.0, d) 1.1, and e) 1.1.

Fig. 6: Singular spectrum obtained by multi-channel SSA (M-SSA) of our model's 54,000-day model integration, in a 3-D subspace. Filled circles show M-SSA eigenvalues, plotted against the dominant frequency associated with the corresponding space-time PCs. Arrows indicate two significant pairs with periods of 19 and 37 days, respectively; note that the two circles in either pair are almost indistinguishable. The confidence intervals correspond to the 5% and 95% percentiles of 100 Monte Carlo simulations of a red-noise process with the same length, variance and lag-one autocorrelation as the model time series being tested; see text and section 4.2 of Ghil et al. (2002) for details.

Fig. 7: Phase composites of the 37-day oscillatory mode, as given by the reconstructed components (RCs) 8 and 9 of the M-SSA. The phase angle  $\varphi$  in the plane spanned by the sum of RCs 8 and 9, on the one hand, and by the derivative of this time series, on the other, is obtained for each day  $t$  of the simulation; the circle  $(0, 2\pi)$  in this plane is then subdivided into eight equally populated arcs of circle, each containing 6750 points  $(\text{RC-8}+\text{RC-9}, \Delta(\text{RC-8}+\text{RC-9}))$  with  $\varphi(t)$  inside that arc. Panels (a)–(d) show four composite maps of all the days  $t$  that fall within four such successive arcs. The four panels shown thus cover one half of the oscillation cycle, while the four additional

panels (not shown) have very similar patterns, with the sign reversed. The composite maps are those of streamfunction anomalies at 500 hPa, as in Fig. 2, with the same plotting conventions and contour intervals.

Fig. 8: Phase velocity in a space of three leading EOFs along the trajectory of RCs 8–9 and 15–16 during two high-amplitude oscillatory spells: (a), (b) and (c) three velocity components (nondimensional units), and d) absolute value for RCs 8–9; (e)–(h) are the corresponding figures for RCs 15–16. Symbols mark the clusters that the trajectory traverses at that moment.

Fig. 9: PDF distribution of the stochastically perturbed Lorenz model, as estimated by a mixture model with  $k=2$ , projected onto a) the  $(X, Y)$  plane, and b) the  $(X, Z)$  plane. All three time series have been normalized by the standard deviation of  $X(t)$ , and filled circles correspond to the two unstable steady states  $W_1$  and  $W_2$  (see text for details). Contours as in Fig. 1 and the heavy solid ellipses correspond to  $1.0\sigma$ . Arrows indicate the preferred transition paths obtained by the method described in section 4b.

Fig. 10: PDF distribution of regime exit angles for the Lorenz model’s two clusters. Asterisks correspond to the line connecting the cluster centroids, and filled triangles correspond to PDF maxima.

# Figures

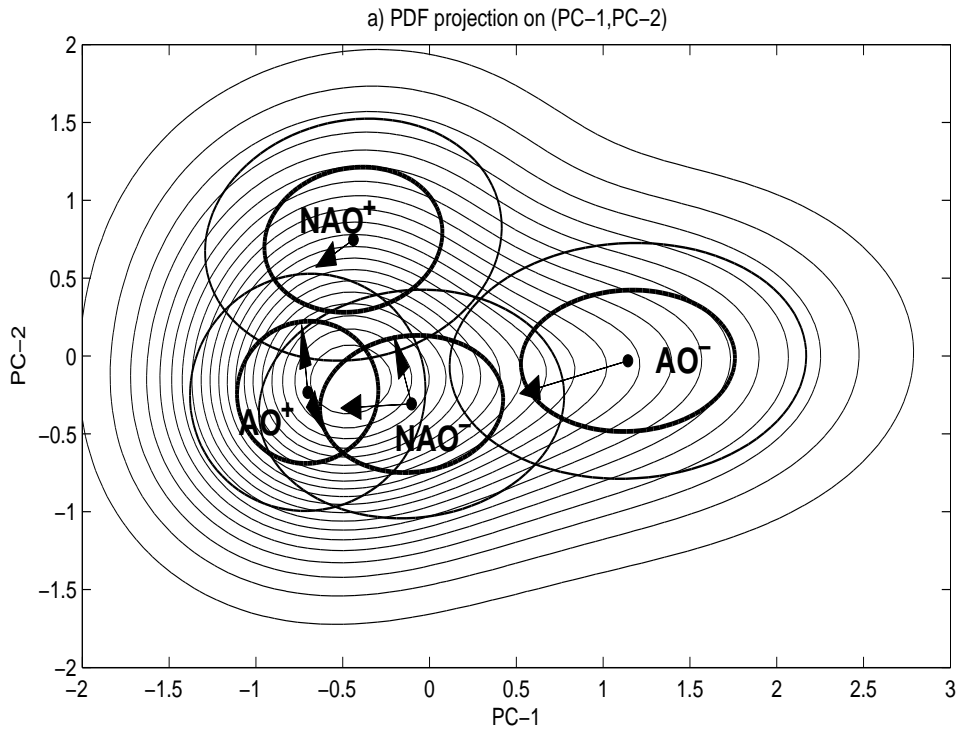


Figure 1

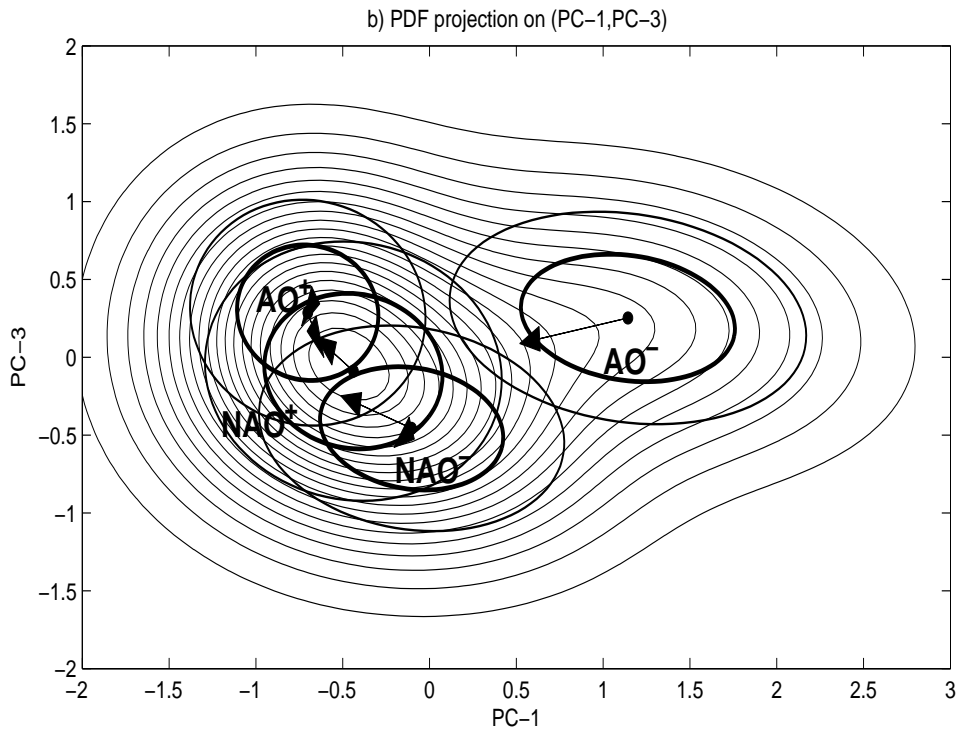


Figure 2

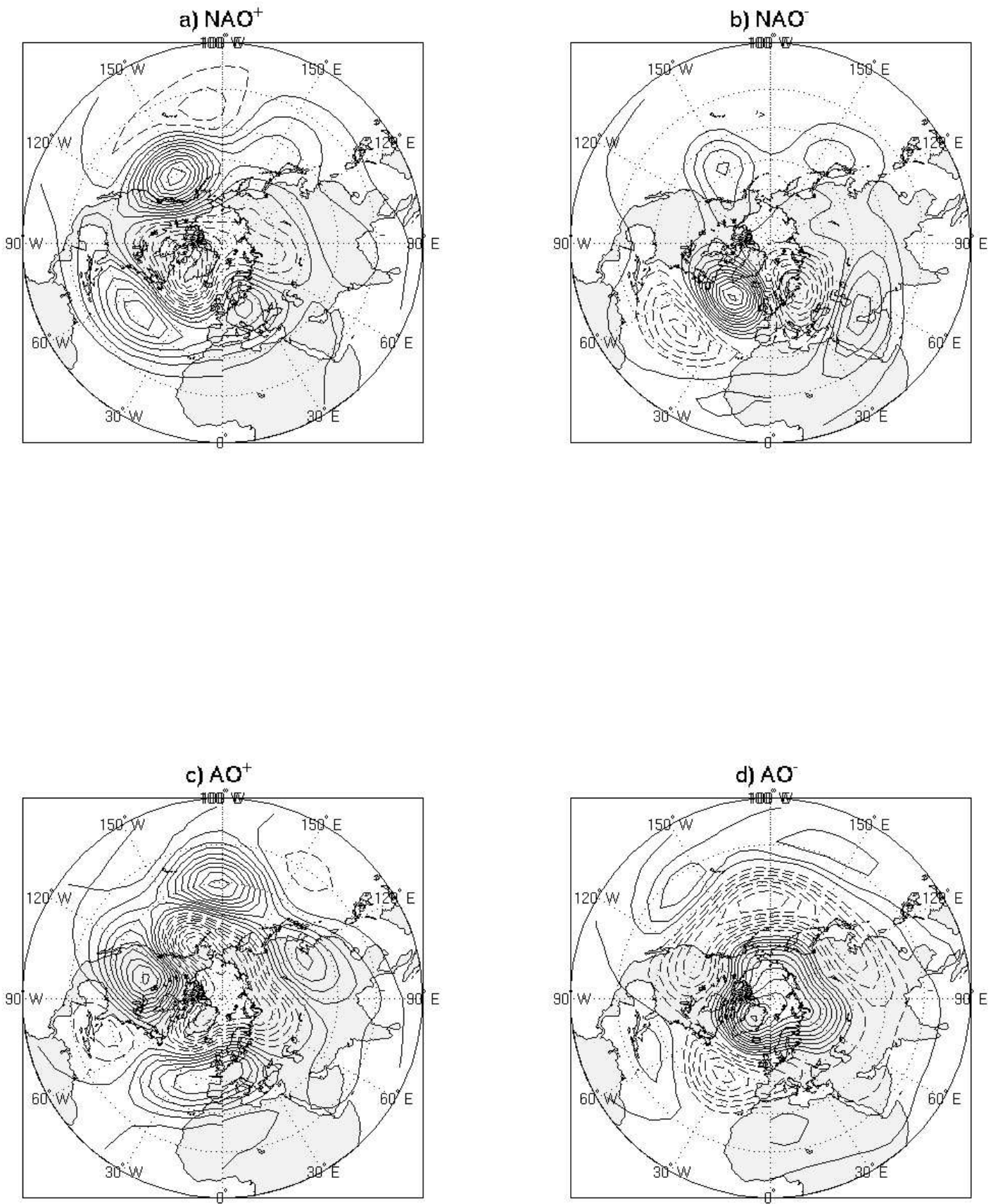


Figure 3

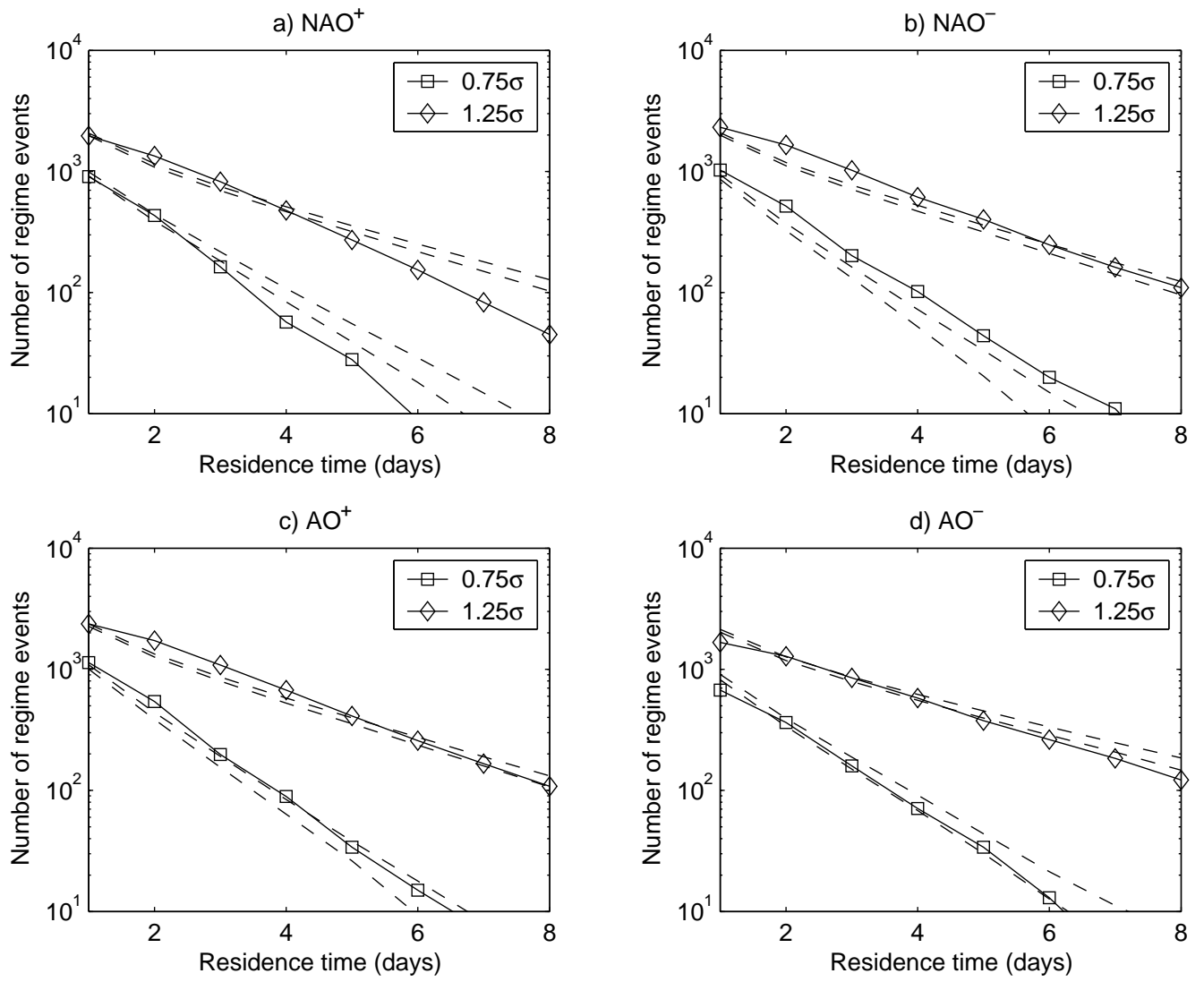


Figure 4

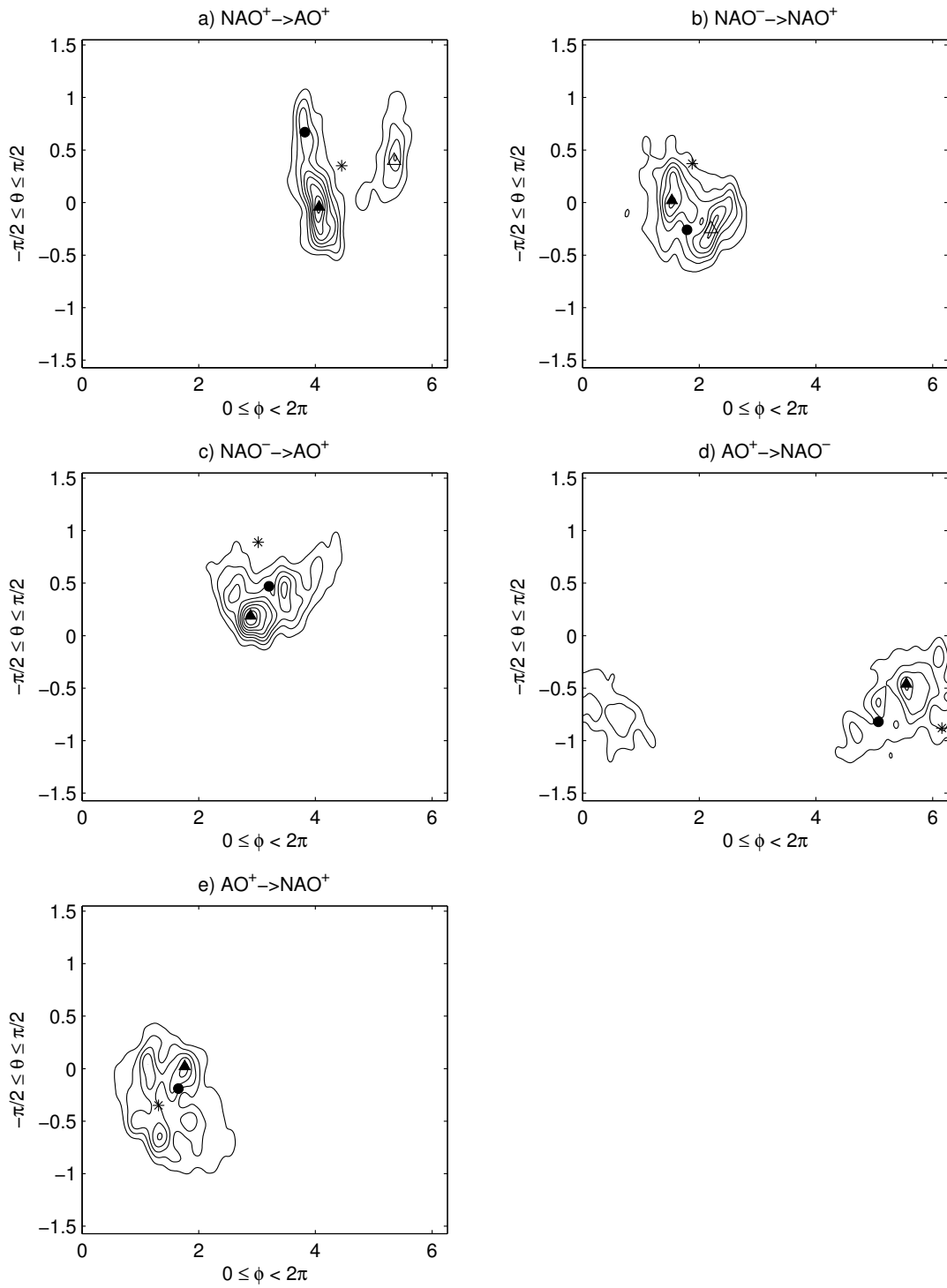


Figure 5

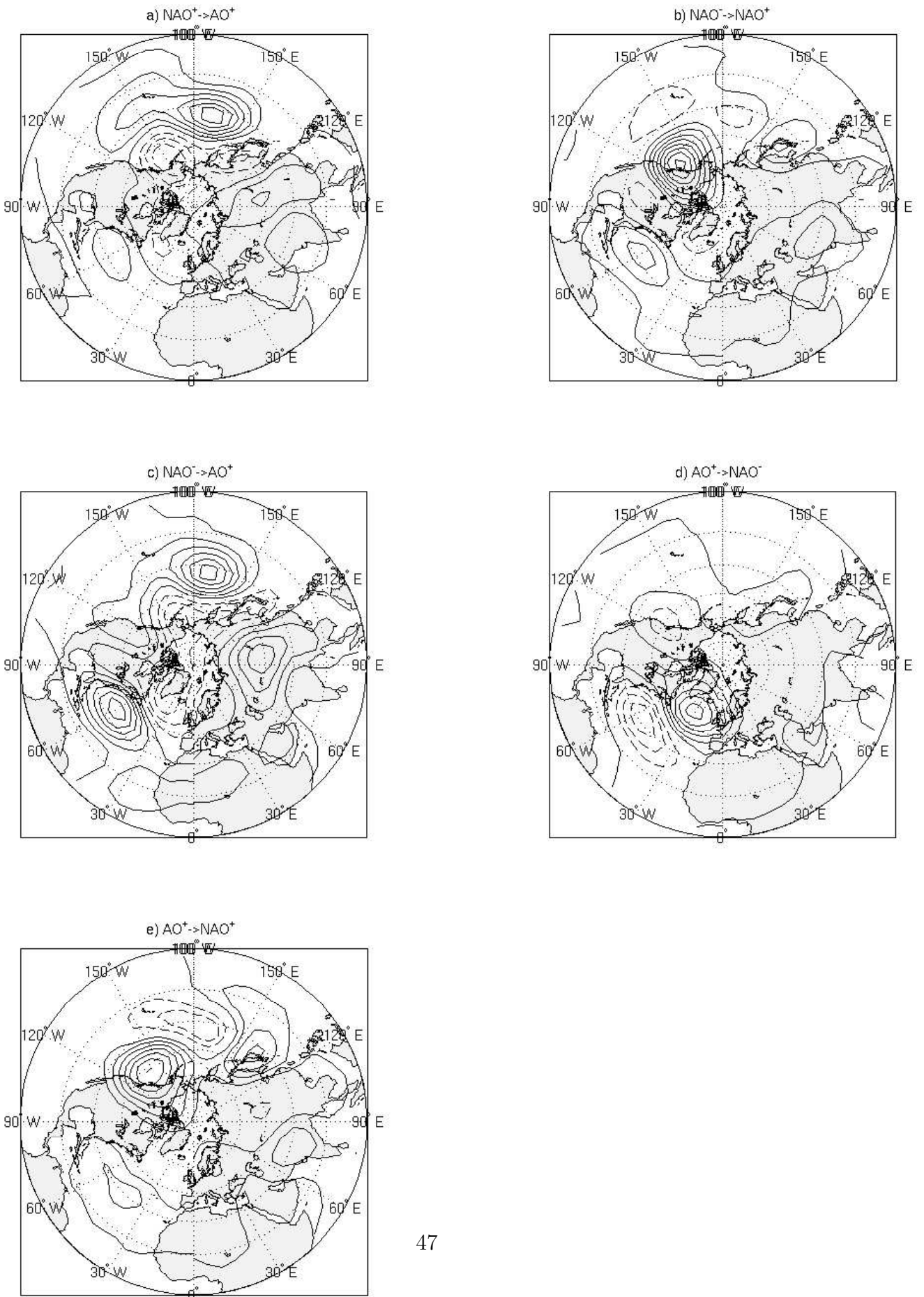


Figure 6

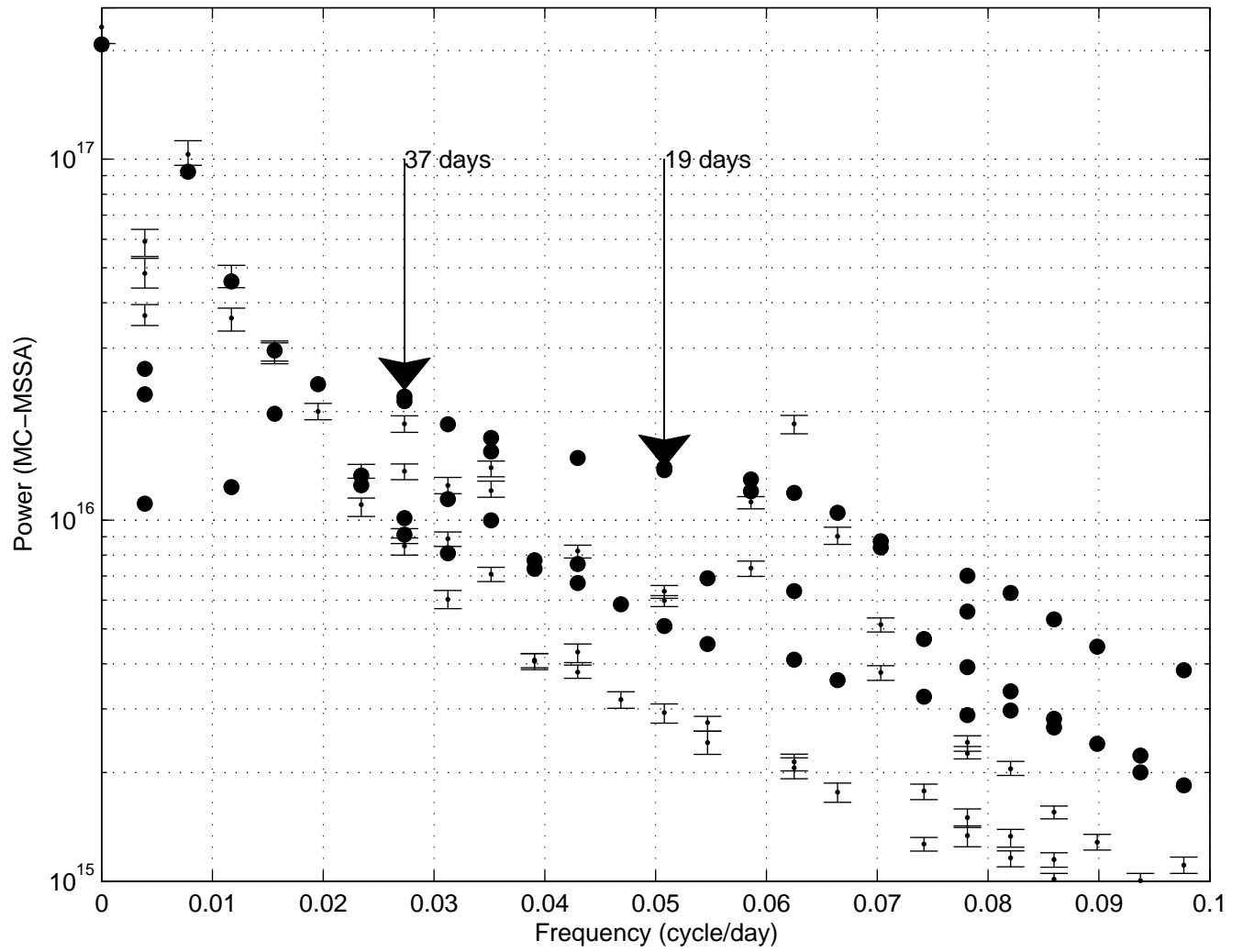
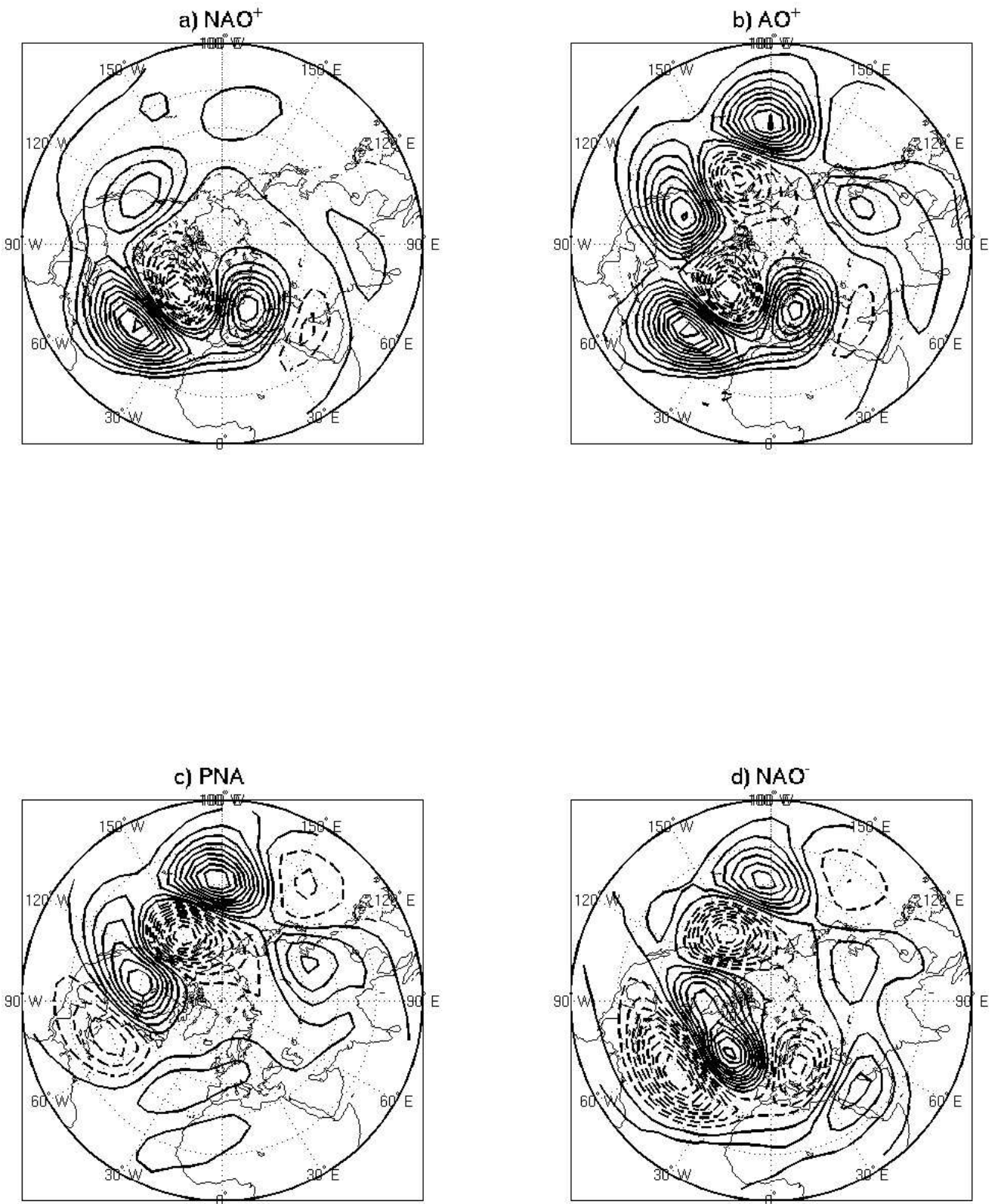
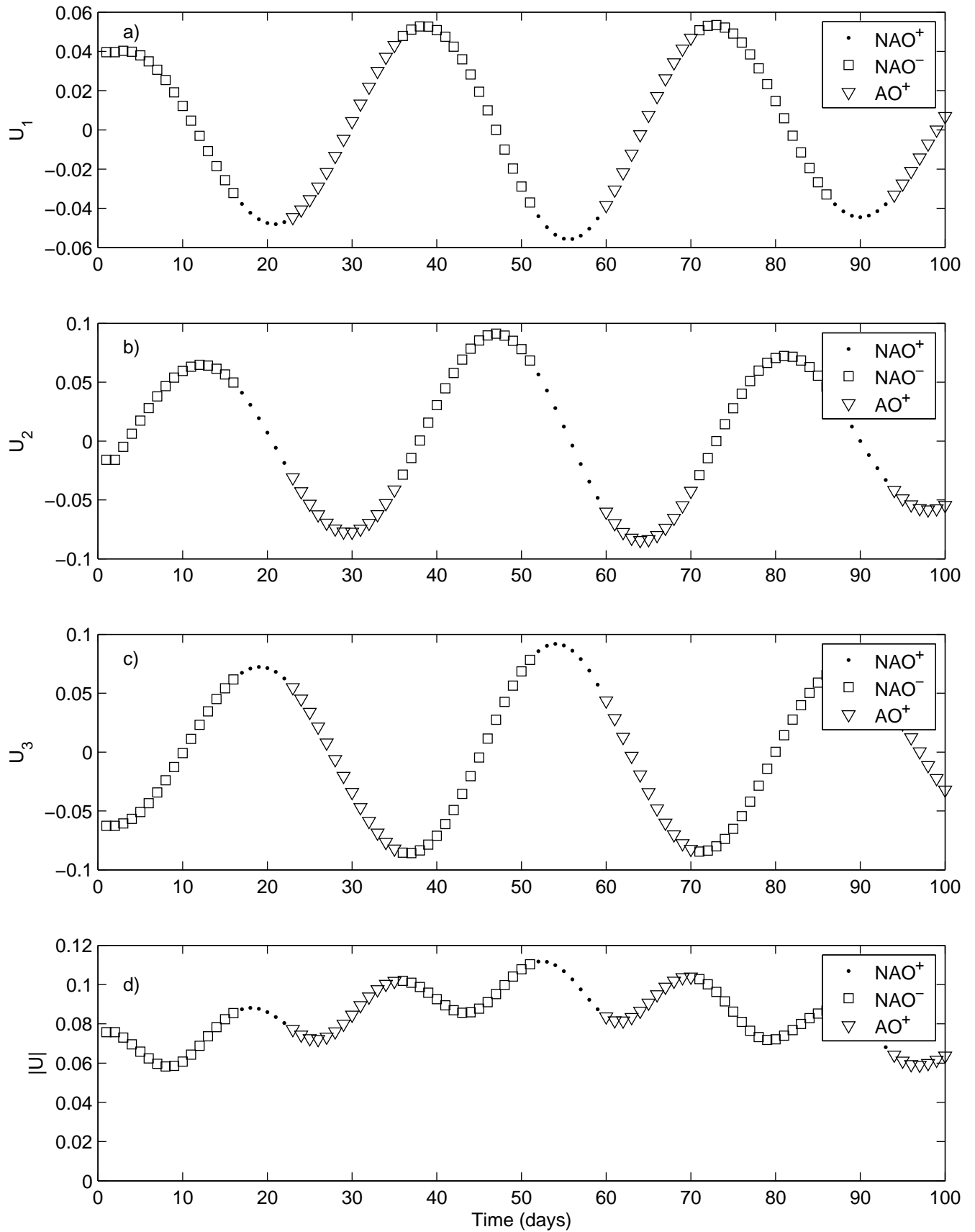


Figure 7



Figures 8a-d



Figures 8e–h

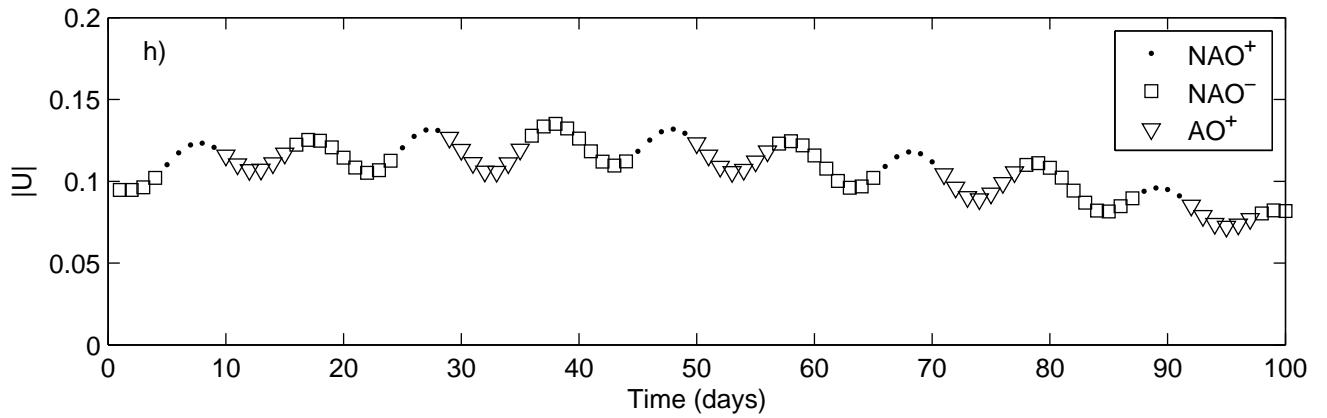
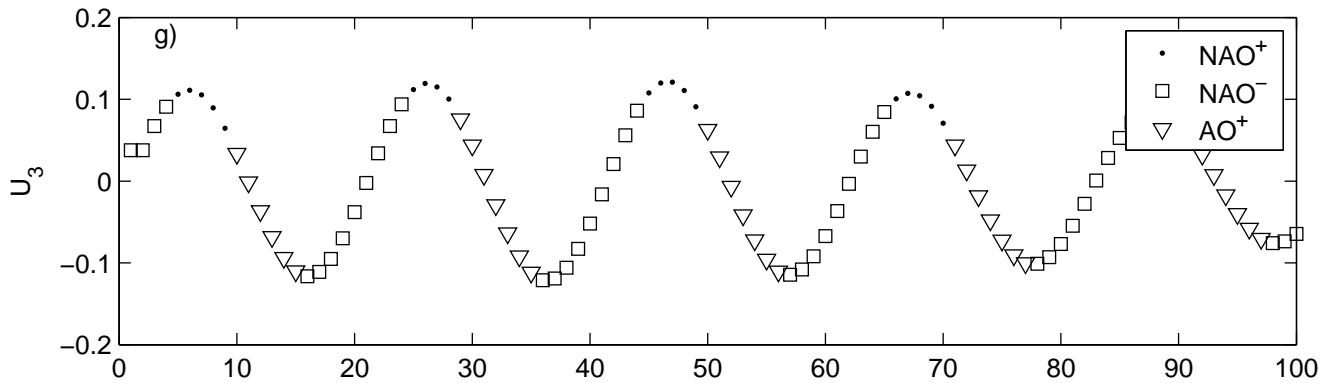
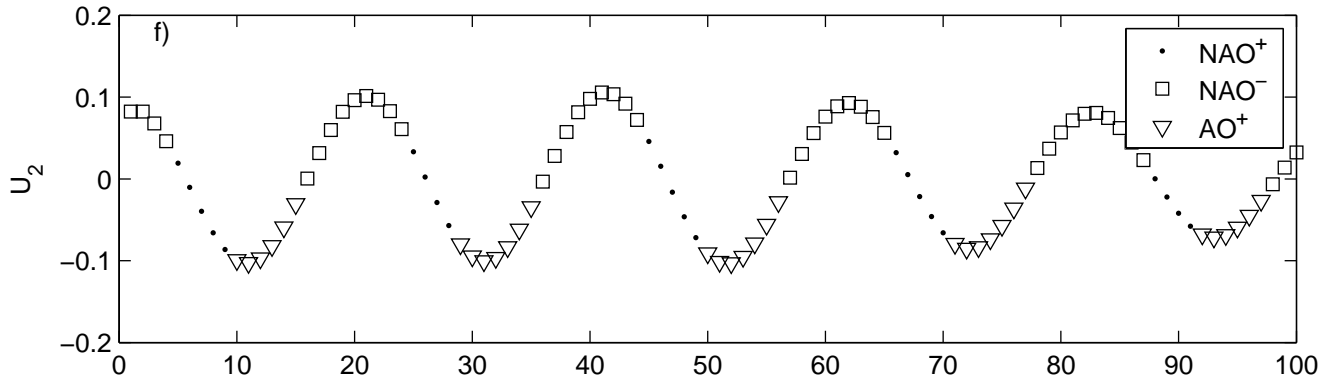
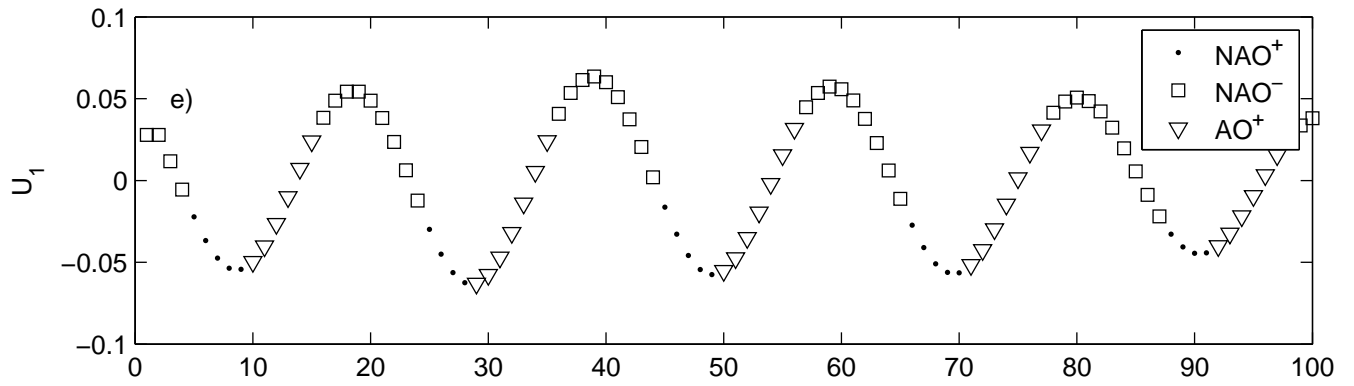


Figure 9

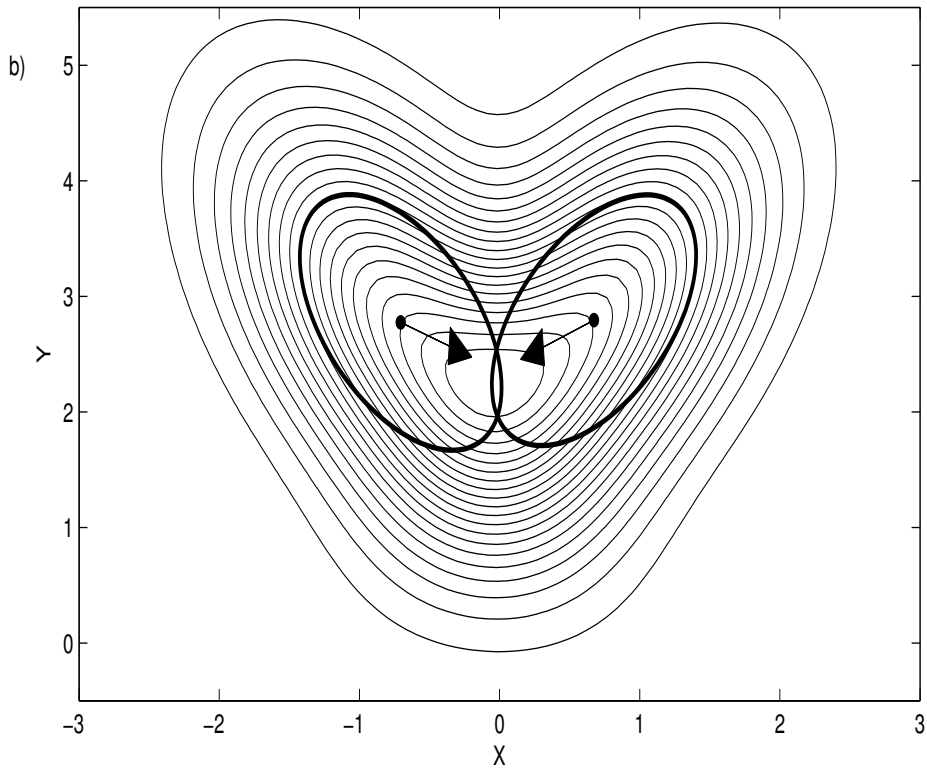
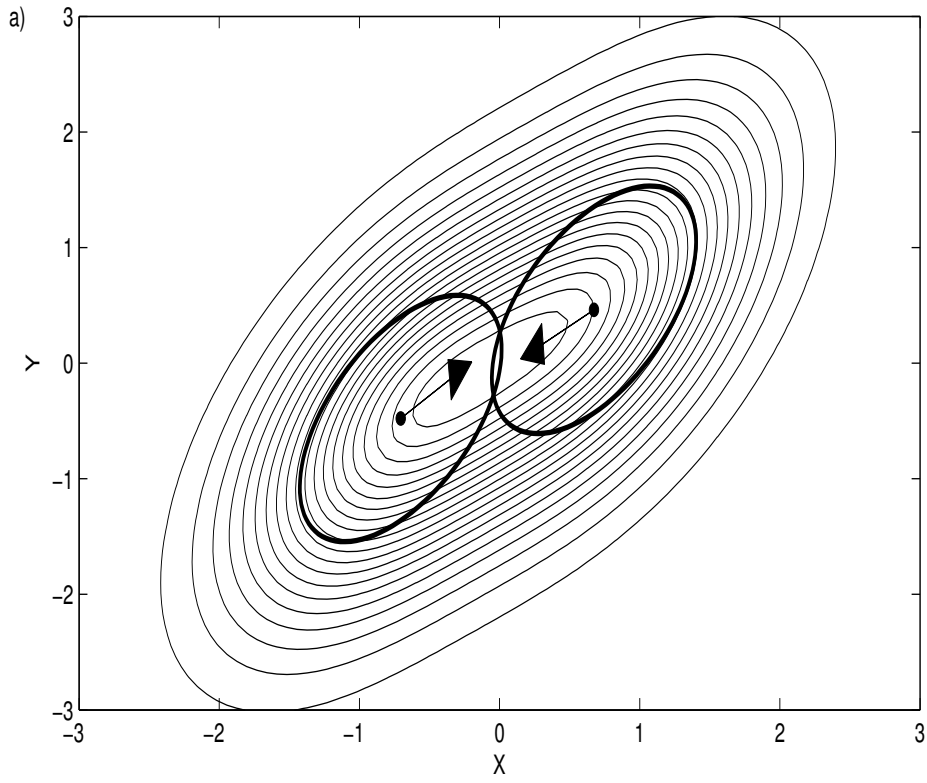


Figure 10

